

# Dual-Hazard Blast and Seismic Behavior of Concrete-Filled Double-Skin Steel Tubes Bridge Pier

P. Fouché, A.M.ASCE<sup>1</sup>; M. Bruneau, F.ASCE<sup>2</sup>; and V. Chiarito, M.ASCE<sup>3</sup>

**Abstract:** The dual-hazard inelastic behavior of concrete-filled double-skin steel tubes (CFDSTs) is experimentally investigated as a substitute to reinforced concrete columns for bridge piers in multihazard applications. Results demonstrate that CFDSTs exhibit substantial toughness and ductility that can help achieve satisfactory performance when exposed to seismic and blast hazards. Under cyclic loading, for all specimens designed as part of this testing program, yielding of the section preceded buckling of the outside tube. The onset of local buckling of the outside tube was not observed until well beyond 4% drift, and failure of all the sections happened generally beyond 7% drift, even when compactness of the outside tube met only the AISC seismic provisions requirements for moderately ductile behavior. In the cyclic tests, although pinching of the hysteresis curve happened during the test, the curves remained stable. For the blast tests, all sections behaved in a ductile manner when subjected to near-contact charges; but for extreme conditions, sections having large voids in their cross section experienced significant denting. Overall, these tests validated the viability of CFDSTs in compliance with AISC compactness requirements for bridge columns in the dual-hazard application considered here. DOI: 10.1061/(ASCE)ST.1943-541X.0001883. © 2017 American Society of Civil Engineers.

**Author keywords:** Concrete-filled double-skin tube columns; Blast resistance; Cyclic behavior; Composite columns; Dual-hazard design; Seismic performance; Local buckling; Testing; Dynamic effects.

## Introduction

Per FEMA (2004), multihazard design requires that designers understand the fundamental characteristics of hazards and how they interact so that design for protection against one hazard becomes integrated with all the other fundamental design demands from the others. Although multihazard is not revolutionary per se, a key aspect of multihazard design is that it looks at how design methods used to protect against the hazards reinforce or are in conflict with one another. When those methods reinforce each other, the estimated demands on the structure will be consistent; and a more uniform level of safety is achievable at reasonable cost. Otherwise, the demands can be in conflict, which may increase costs. In that perspective, the development of integrated multihazard bridge systems is desirable. Earthquakes and explosions are worth considering from a dual-hazard perspective, as structural survival to both hazards relies on large inelastic response (AASHTO 2012; DoD 2008).

There is a continued concern that bridges may become prime targets for terrorists (Williamson and Winget 2005). This concern is justified, as threats have already been received against landmark bridges across the nation. However, because common highway bridges are not as closely monitored as landmark bridges, they are

more accessible targets; and in many instances their destruction can provoke significant casualties and profoundly affect the economic circuit built around those transportation infrastructures. Because many of these bridges are also built in areas prone to earthquakes, dual-hazard design is required.

Typically, bridge columns are the most vulnerable component of a bridge system, and their failure generally leads to partial or complete failure of the structure itself. Frequently, columns are readily accessible, which makes them a likely target in a terrorist attack; and they are typically relied upon to protect the structure during earthquakes by working as structural fuses that dissipate the seismic energy. Bridge piers can also be subjected to vehicle collision or exposed to fires. Columns that are made of concrete-filled, double-skin steel tubes (CFDSTs), because of their inherent structural qualities of higher strength, substantial toughness, and ductility, can help achieve satisfactory performance when exposed to these hazards. CFDSTs are also attractive because of the cost saving they can generate by permitting accelerated bridge constructions. Therefore, CFDSTs are investigated here as a substitute to reinforced concrete columns for bridge piers erected in multiple-hazard-prone environments. Emphasis here is on the bihazard environment constituted by earthquake loading and blast overpressures. The fire resistance of CFDST columns is already known to be excellent, as described elsewhere (e.g., Lu et al. 2010; Imani et al. 2015a, b).

## Concrete-Filled Double-Skin Steel Tubes

CFDSTs are a kind of steel-concrete-steel sandwich section formed by two concentric steel tubes separated by a concrete filler, as shown in Fig. 1. That configuration seeks to draw upon the benefits in strength, toughness, and stiffness derived from steel-sandwich construction by placing the steel at the periphery of a filler material. Attributable to the cylindrical shape of this sandwich construction, a void exists in its center. This allows the resulting cross section to

<sup>1</sup>Consultant, Haiti; formerly, Graduate Research Assistant, Dept. of Civil, Structural and Environmental Engineering, Univ. at Buffalo, Buffalo, NY 14260.

<sup>2</sup>Professor, Dept. of Civil, Structural and Environmental Engineering, Univ. at Buffalo, Buffalo, NY 14260 (corresponding author). ORCID: <https://orcid.org/0000-0003-1170-468X>. E-mail: [bruneau@buffalo.edu](mailto:bruneau@buffalo.edu)

<sup>3</sup>Research Structural Engineer, CEERD-GSS, 3909 Halls Ferry Rd., U.S. Army Engineer Research and Development Center, Vicksburg, MS 39180-6199. E-mail: [Vincent.p.chiarito@uace.army.mil](mailto:Vincent.p.chiarito@uace.army.mil)

Note. This manuscript was submitted on June 28, 2016; approved on May 9, 2017; published online on September 18, 2017. Discussion period open until February 18, 2018; separate discussions must be submitted for individual papers. This paper is part of the *Journal of Structural Engineering*, © ASCE, ISSN 0733-9445.

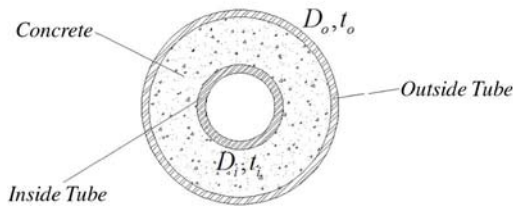


Fig. 1. CFDST section

concentrate materials where needed for optimal performance: the outside skin at the periphery of the section provides strength and stiffness, the inside skin enhances ductility, and the concrete between provides strength and local and overall stability to the system. Also, because of the obvious similarities with concrete-filled tubes (CFSTs), the concrete core is expected to be confined by the tubes and will provide, in return, support to the tube skins against local buckling. That synergy between the tubes and the core in resisting loads and providing ductile response is expected to result in a section with good structural and energy dissipation qualities. Using CFDSTs can also result in slender columns with less surface to be exposed to blast overpressures than reinforced concrete columns or equivalent flexural strength. The inner tube also provides desirable blast resistant features and strength for fire resistance (Imani et al. 2015a, b).

CFDSTs were studied by Montague (1975) as a substitute for steel shells subjected to external pressure, by Shakir-Khalil (1991) under monotonic lateral loading, and by Wei et al. (1995) for use in the petroleum industry to cope with the local and global stability concerns that often prevent steel tubes from developing their full yield strength (API 1989). However, studies on CFDSTs remain scarce, particularly with respect to cyclic inelastic behavior and blast resistance. Experimental and analytical studies have investigated the behavior of CFDST (and tapered CFDST in some cases) in compression (Wei et al. 1995; Uenaka et al. 2010; Huang et al. 2010; Yuan and Yang 2013; Pagaoulatou et al. 2014; Li et al. 2012, 2013; Zhao et al. 2010; Zhong et al. 2004), tension (Li et al. 2014a, b), torsion (Huang et al. 2013), monotonically-applied compression and flexure (Tao et al. 2004; Tao and Han 2006), and fire (Lu et al. 2010; Imani et al. 2015a, b).

Limited cyclic tests to date (Tao et al. 2004; Lin and Tsai 2001; Han et al. 2006) on beam-column elements with high slenderness ratio and variable level of axial load have established that CFDSTs can provide strength and deformation capacity that emulate those of CFSTs even with diameter-to-thickness ratios in excess of the limit currently imposed by AISC 341-10 [(AISC 2010); 87 for grade 50 steel] on concrete-filled circular steel sections (ratio as high as 100–150:1 for the outer tubes and 90:1 for the inner tube were studied). Han et al. (2006, 2009) showed that CFDSTs exhibit some drop in ductility with increases in axial load, based on results from specimens tested at axial load levels of 0.23, 0.43, and 0.63 of the ultimate axial capacity of the section (which would be significantly higher than typically found in bridge columns). Recent research on CFDSTs (and CFSTs) having ultra-high-strength outer steel tubes [with yield stress in excess of 700 MPa (100 ksi)] allowed the development of greater ductility under high axial loads but found that the use of higher strength decreased this ductile capacity (Hsiao et al. 2015).

Research on the blast resistance of CFDST is even scarcer. Zhang et al. (2016), in tests contemporaneous to those reported here, subjected CFDSTs having ultra-high-performance concrete averaging compressive strength of 170 MPa (25 ksi) to applied

axial forces and blast pressures that produced modest levels of inelastic demands on the members with “no visible buckling nor ruptures found on the steel tubes.”

In light of the limited data available on both the seismic and blast resistance of CFDST, the experimental results presented here provide valuable data on this topic that can be useful in future studies to expand knowledge on the inelastic ultimate behavior of CFDST.

As no closed-form equations were found in the literature for either the flexural strength of CFDSTs or the combined axial and flexural loadings, a set of equations was derived for comparison with experimental results. Equations for flexural strength are presented in the Appendix. However, because of space constraints here, the set of multiple equations for combined axial and flexural loadings is presented in Fouché and Bruneau (2014).

## Specimen Design

In light of the limited knowledge available, to investigate a broader range of cross-section parameters and to validate the seismic and blast performance of CFDST sections, five quarter-scale CFDST column specimens, with geometry and section parameters representative of different arrangements of the tube shells and consistent with the conditions expected in full-scale applications, were instrumented and subjected to cyclic loading. In addition, 12 quarter-scale column specimens (grouped into three bents of four columns each) were subjected to blast loading: eight were blast tested at the University at Buffalo’s outdoor Experimental Campus for Large Infrastructure Protection, Sustainability and Enhancement (i.e., the ECLIPSE testing facility), and another four were tested later at the Big Black Testing Site of the U.S. Army Engineer Research and Development Center (ERDC) in Vicksburg, Mississippi. Note that properly-designed scale testing has gained substantial acceptance in blast engineering over the past decade and has been proven to provide reliable results and key knowledge in understanding the behavior of structures subjected to blast (e.g., Woodson and Baylot 1999; Baylot and Rickman 2007; Williams et al. 2008; Orton et al. 2014; Bruhl and Varma 2015; Burrell et al. 2015). The work conducted here was performed in the same mindset.

The objective of the cyclic test series was to evaluate experimentally the behavior of CFDSTs in terms of ductility and behavior up to failure (which typically occurs caused by low-cycle fatigue) in the perspective of seismic response. The objective of the blast-test series was to assess experimentally how blast performance is affected by various design and geometric parameters (e.g., larger versus smaller void, tube compactness with respect to specified limits for highly ductile versus moderately ductile behavior).

Design of the specimens was based on the analytical studies of multihazard full-scale bridges presented in Fouché and Bruneau (2014). The specimens selected for this test series were quarter-scale models of some of the prototype CFDSTs designed as part

**Table 1.** Cyclic Pushover Test Specimens

Designation	Specimen	$H$ (in.)	$D_i$ (in.)	$D_o$ (in.)	$t_i$ (in.)	$t_o$ (in.)	$\frac{D_i}{t_i}$	$\frac{D_o}{t_o}$	$\chi$	Ductility designation	
										Inside tube	Outside tube
17_72_33	S1	67.25	2	6	0.116	0.083	17.24	72.29	0.33	HD	MD
16_70_25	S2	67.25	2	8	0.123	0.114	16.26	70.18	0.25	HD	MD
22_50_38	S3	71.25	2.5	6.625	0.114	0.133	21.93	49.81	0.38	HD	HD
26_48_33	S4	67.25	2	6	0.076	0.117	26.32	48.00	0.33	HD	HD
56_70_63	S5	67.25	5	8	0.09	0.114	55.56	70.18	0.63	HD	MD

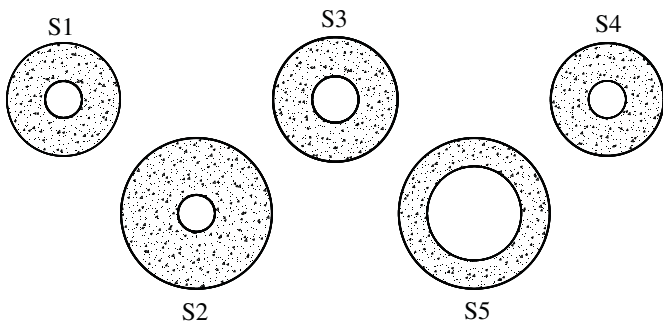
of those studies. Those specimens met the compactness limits set by the AISC 341-10 *Seismic Provisions* (AISC 2010) to achieve ductile behavior for concrete-filled composite sections. The decision to comply with those limits stemmed from the fact that CFDSTs are essentially concrete-filled sections quite similar to CFSTs and, arguably, should be subjected to the same compactness limits. If this holds true, CFDSTs meeting those requirements should, accordingly and like their CFST counterparts, develop the strength and ductility demands expected of them under earthquake and blast loading. For the current research, this line of reasoning resulted in sections that combined inside and outside tubes with different compactness and corresponding expected ductility capacities as defined by the AISC *Seismic Provisions* (AISC 2010).

The main geometric features of the specimens subjected to cyclic loading, labeled S1–S5, are presented in Table 1. In Table 1, the numbers used in the first column to designate the specimens (e.g., 17\_72\_33) represent in that order the diameter-to-thickness ratios for the inside and outside tubes rounded to the nearest integer (i.e., 17 and 72) and the void ratio in percentage, (i.e., 33%), defined as the ratio of the inside to the outside diameter. The third column gives information on the cantilever height ( $H$ ) for each specimen; all specimens but Specimen S3 have the same height. The other parameters contained in this table are the diameter of

the outside tube ( $D_o$ ), the diameter of the inside tube ( $D_i$ ), the thicknesses of the inner ( $t_i$ ) and the outer ( $t_o$ ) tubes, the diameter-to-thickness ratios for the inner ( $D_i/t_i$ ) and the outer ( $D_o/t_o$ ) tubes, and the void ratio ( $\chi = D_i/D_o$ ). The acronyms HD and MD in the last column of this table, respectively, refer to the AISC 341-10 (AISC 2010) designations of *highly ductile* and *moderately ductile* that limit the  $D/t$  value of the tubes to  $0.076E/f_y = 68.9$  and  $0.15E/f_y = 135.9$ , respectively, for material values of  $F_y = 32$  ksi (220 MPa) and  $E = 29,000$  ksi (200,000 MPa). In the perspective of seismic design, note here that the outside tubes of Specimens S1, S2, and S5 have compactness deemed sufficient to develop only moderate levels of ductility, whereas the other two specimens satisfy the designation for high level of ductility.

Note that Specimens S1 and S4 have the same outside and inside tube diameters, but the thicknesses of their outside and inside tubes are interchanged to produce two section configurations with the same void ratio but different overall expected ductility (the outside tube of S1 is MD, whereas that of S4 is HD). Note also that Specimens S2 and S5 were chosen with outside tube diameters that are identical but with inside tube diameters leading to sections having small and large void ratios (0.25 versus 0.63), respectively, yet having the same ductility designation of MD. Specimen S4 was chosen to fall near the middle of the spectrum of void ratios considered for the specimens. For a visual reference, Fig. 2 provides scaled drawings of the cross sections of the different specimens that were tested.

Of the eight specimens tested at the *ECLIPSE* testing facility, five were CFDSTs similar to those subjected to cyclic testing, and one was a CFST with a specified outside tube diameter of 152 mm (6 in.). The other two were selected to extend the spectrum of void ratios from 25 to 63%. Tables 2 and 3 summarize the main geometric and section features of the specimens. The notation used for the specimen names is consistent with that used earlier, except that the prefix B is used instead of S to designate the specimens of this blast test series. For the ERDC tests, the two sections with the largest void ratios from the *ECLIPSE* series were modified to have diameter-to-thickness ratios of their outside tubes such that they met the AISC 341 (AISC 2010) requirements for highly ductile members, based on the premise that increasing the compactness

**Fig. 2.** Selected cross sections**Table 2.** *ECLIPSE* Tests Specimens

Specimen	Column designation	$H$ (mm)	$D_i$ (mm)	$D_o$ (mm)	$t_i$ (mm)	$t_o$ (mm)	Void ratio	Ductility	
								Inside tube	Outside tube
17_72_33	B1	1,500	50.80	152.4	2.9464	2.1082	0.33	HD	MD
16_70_25	B3	1,500	50.80	203.2	3.1242	2.8956	0.25	HD	MD
56_70_63	B7	1,500	127	203.2	2.2860	2.8956	0.63	HD	MD
26_48_33	B5	1,500	50.80	152.4	1.9304	3.1750	0.33	HD	HD
20_73_42	B2	1,500	63.50	152.4	3.1750	2.0828	0.42	HD	MD
22_50_38	B4	1,500	63.5	168.3	2.8956	3.3782	0.38	HD	HD
33_94_50	B6	1,500	101.6	203.2	3.0480	2.1590	0.50	HD	MD
—	B8	1,500	—	152.4	—	3.0480	0	—	HD

**Table 3. ERDC Tests Specimens**

Specimen	Column designation	H (mm)	D <sub>i</sub> (mm)	D <sub>o</sub> (mm)	t <sub>i</sub> (mm)	t <sub>o</sub> (mm)	Void ratio	Ductility	
								Inside tube	Outside tube
21_50_42	B9	1,500	63.5	151.5	3.0480	3.0480	0.42	HD	HD
21_51_38	B10	1,500	63.5	165.3	3.0226	3.2512	0.38	HD	HD
30_41_50	B11	1,500	101.0	201.5	3.3528	4.9022	0.50	HD	HD
40_42_62	B12	1,500	124.6	201.4	3.1496	4.8006	0.62	HD	HD

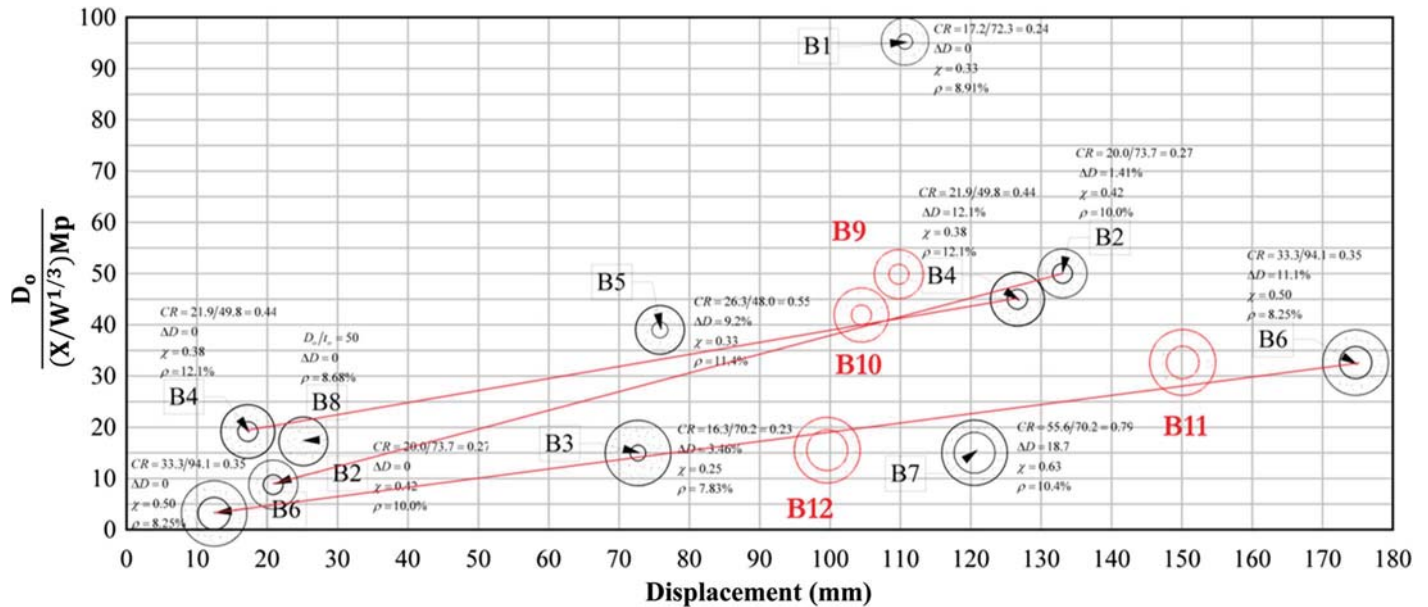


**Fig. 3. Normalized demand/capacity as a function of displacement response**

of the outside tube could help minimize denting while keeping large void ratios. The remaining two specimens tested at ERDC were similar to B2 and B4 and were intended to gather complementary data on specimens with moderate void ratio. Fig. 3 was used to guide the selection of specimens to be tested at ERDC by showing the maximum lateral deformation of the specimens (that can be related to plastic rotation using geometry and height of the point of maximum deformation) as a function of demand/capacity ratios for the blast-tested specimens. Note that, in this figure, the demand/capacity ratio was nonconventional but was expressed, nonetheless, in a manner informative for showing relative trends within the entire series of tests. The ordinate of that figure was chosen by performing a relative comparison of a uniformly distributed load  $\omega_u$ , divided by the corresponding value for the plastic mechanism (equal to  $28.8M_p/L^2$  for the position of the charge considered), and by taking  $\omega_u = kpD_o$ , where  $p$  is the blast pressure,  $D_o$  is the column diameter on which pressure is acting, and  $k$  is a constant depending on column cross-section shape). Using a crude first estimate of the pressure as  $p = 1/Z^3$  (kPa) for simplicity and eliminating constants from the ratio, the following demand/capacity ratio was obtained:  $\omega_u/(M_p/L^2)$ , leading to  $(D_o/Z^3)/(M_p/L^2)$ , itself leading to  $D_o \times L^2 / [(X/W)^{1/3} \times M_p]$ , and to the ordinate of Fig. 3 when eliminating  $L$  (which was the same here for all specimens). Again, note that the sole purpose of Fig. 3 was to illustrate graphically (and relatively) how the ERDC tests were intended to fill gaps in the *ECLIPSE* set of results. For that reason, in Fig. 3, maximum deformations are those *measured* for the *ECLIPSE* tests and *predicted* for the ERDC tests.

### Materials

The tubes used to build the test specimens were electric resistance welded tubes. Those products are available in cold rolled strip (16 gauge and lighter) and hot rolled strip [2.1-mm-(0.083-in.)-thick wall and heavier]. The steel used in their manufacturing complies with ASTM A513 type 1 or 2 [ASTM A513/A513M-15 (ASTM 2015)]. Those tubes nominally have a yield strength of 4.6 MPa (32 ksi), a tensile strength of 6.5 MPa (45 ksi), and 15% minimum elongation at failure. The experimentally measured stress-strain curves for those specimens are provided in Fig. 4 for coupons obtained from extra lengths that were cut from each tube (both inner and outer ones) before the tests. Pieces of those extra lengths of tube were flattened first, and coupons were machined from them. By this procedure, those coupons might have been cold-worked, which may explain why not all of them reached the minimum required elongation at failure. It is also worth noting that no defined yield plateau was obtained for any of the tested coupons; consequently, the 0.2% offset method was used to determine the nominal yield strength of the section for all purposes.

Casting of the concrete for the seismic and blast specimens occurred at the same time. To accelerate construction, prevent segregation of the concrete, and avoid the need for compaction, a self-placing concrete with an average compressive stress of 0.73 MPa (5.0 ksi), a maximum aggregate size of 13 mm (1/2 in.), and a spread during the slump test between 457 and 762 mm (18 and 30 in.) was used for this application. Concrete cylinders cast during the construction and tested 42 days after the placement gave an

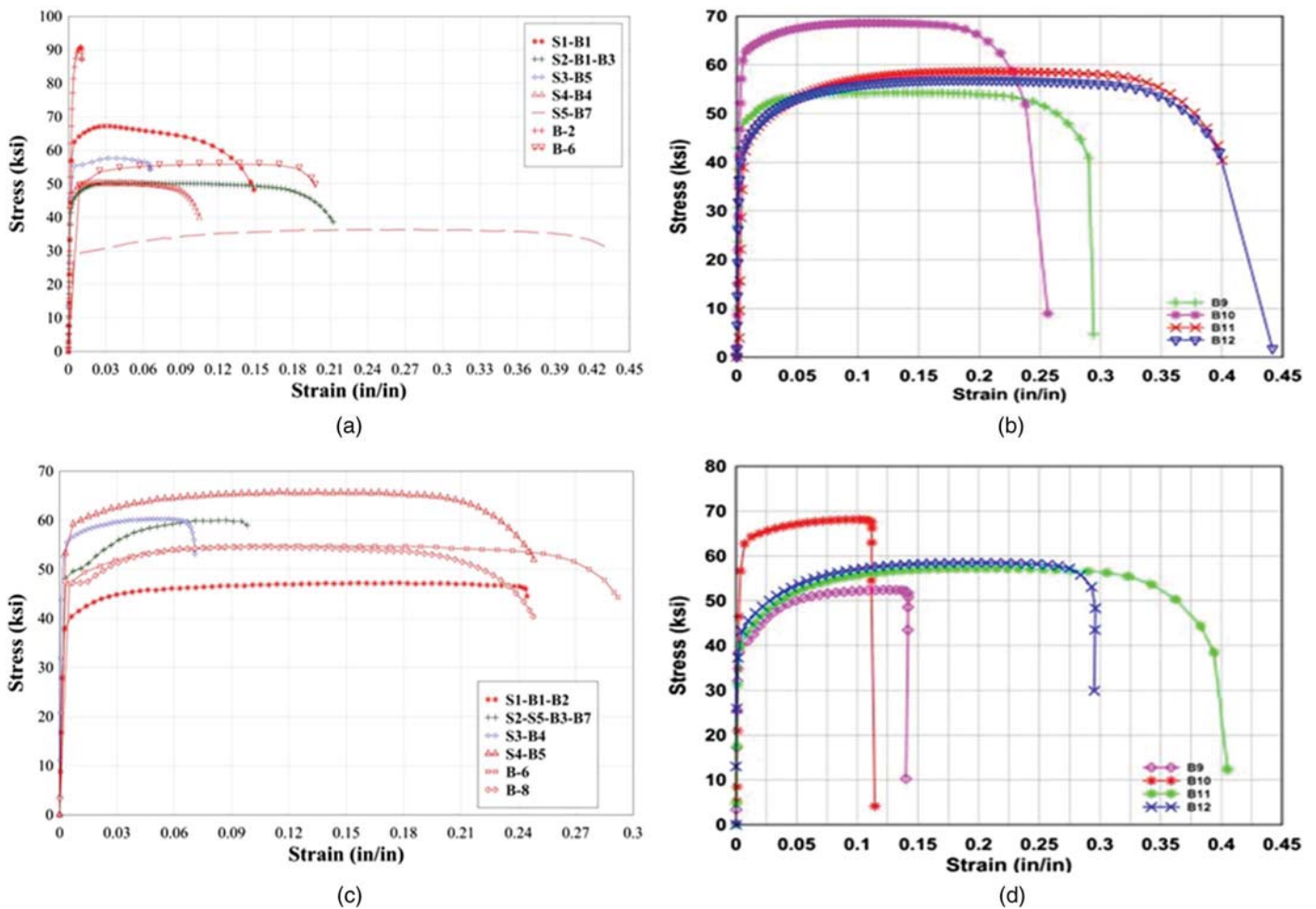


Fig. 4. Stress strain curve from steel coupons: (a and b) inside tubes; (c and d) outside tubes

average cylinder strength of 0.78 MPa (5.4 ksi) with a standard deviation of 0.014 MPa (0.1 ksi). Using the ACI Committee 211 (ACI 1992) relationship, compressive strength on the test days was predicted to be 0.82–0.83 MPa (5.63–5.71 ksi) for the various specimens tested (a 5% difference at most).

### Calculated Section Strengths

Because all specimens were made of compact tube elements, it was expected that they would reach their full nominal plastic strength ( $M_p$ ). The nominal plastic strength of each of the specimens was calculated using the equations presented in the Appendix. Those equations assumed that steel components reach their nominal yield strength,  $F_y$ , and that all concrete in compression reaches its full strength,  $f'_c$ , but it neglects the concrete in the tensile region. Note that although the plastic stress distribution principles in AISC 341-10 (AISC 2010) recommend using 95% of  $f'_c$ , CFDSTs are expected to develop confinement, which justified ignoring this reduction. Resulting values are in Tables 4 and 5.

### Description of the Experimental Setup

The column specimens in the cyclic tests were 2,038-mm (80.25-in.)-tall cantilevers having a built-up steel component at their base to provide a means to connect the specimen to the top flange of a W14 × 211 strong beam that was part of a reaction

Table 4. Calculated Strengths of S Specimens;  $f'_c = 38$  MPa (5.4 ksi)

Designation	Specimen	$F_{yo}$ [ksi (MPa)]	$F_{yi}$ [ksi (MPa)]	$M_p$ [kip-in (kN-mm)]
17_72_33	S1	40.00 (279)	61.30 (428)	207.46 (23,443)
16_70_25	S2	49.62 (346)	45.20 (315)	514.98 (58,192)
22_50_38	S3	56.00 (391)	51.04 (356)	446.09 (50,408)
26_48_33	S4	57.40 (401)	46.98 (328)	314.61 (35,551)
56_70_63	S5	49.62 (346)	28.6 (200)	532.50 (60,173)

Table 5. Calculated Strengths of B Specimens

Designation	Specimen	$F_c'$ (MPa)	$F_{yo}$ (MPa)	$F_{yi}$ (MPa)	$M_p$ (kN-m)
17_72_33	B1	37.23	275.65	307.23	26.51
16_70_25	B3	37.23	330.95	307.23	67.99
56_70_63	B7	37.23	330.95	220.63	71.72
26_48_33	B5	37.23	379.21	379.21	43.62
20_73_42	B2	37.23	275.65	558.48	33.19
22_50_38	B4	37.23	368.87	325.50	57.91
33_94_50	B6	37.23	321.09	315.99	62.26
21_50_42	B9	37.23	396.17	406.51	46.22
21_51_38	B10	37.23	470.50	483.64	72.91
30_41_50	B11	37.23	389.28	405.34	127.97
40_42_62	B12	37.23	396.17	406.51	136.08

frame. Details of the built-up steel component are provided in Fouché and Bruneau (2014) along with details for connecting the top of the cantilever specimens to a horizontal actuator having swivels at both its ends. Note that the built-up base was heavily instrumented to measure its deformations and accordingly correct measured column deflections to obtain results for a rigidly fixed base. Data recorded during the tests showed that this built-up detail added approximately 5–10% to typical specimen lateral deformations at maximum strength.

The test setup in the blast test series was similar to the one found in Fujikura and Bruneau (2011). Concrete encased built-up steel sections were used as cap and foundation beams of each

multicolumn bent. The built-up steel sections were similar to the box sections described for the seismic test but spanned the entire length of the bent. For design purposes, the cap beam was made stronger than the foundation beam and was the same for all blast test series. This is because the design of the cap beam was controlled by blast overpressures, whereas the foundation beam was designed for the capacity of the strongest specimen attached to it. Each bent contained four equally spaced columns [Figs. 5(a and b)]. Because the test procedure called for the columns to be tested in turn, the spacing between the columns was selected such that, when any column was being tested, the neighboring columns would remain elastic. It was found that a spacing of approximately

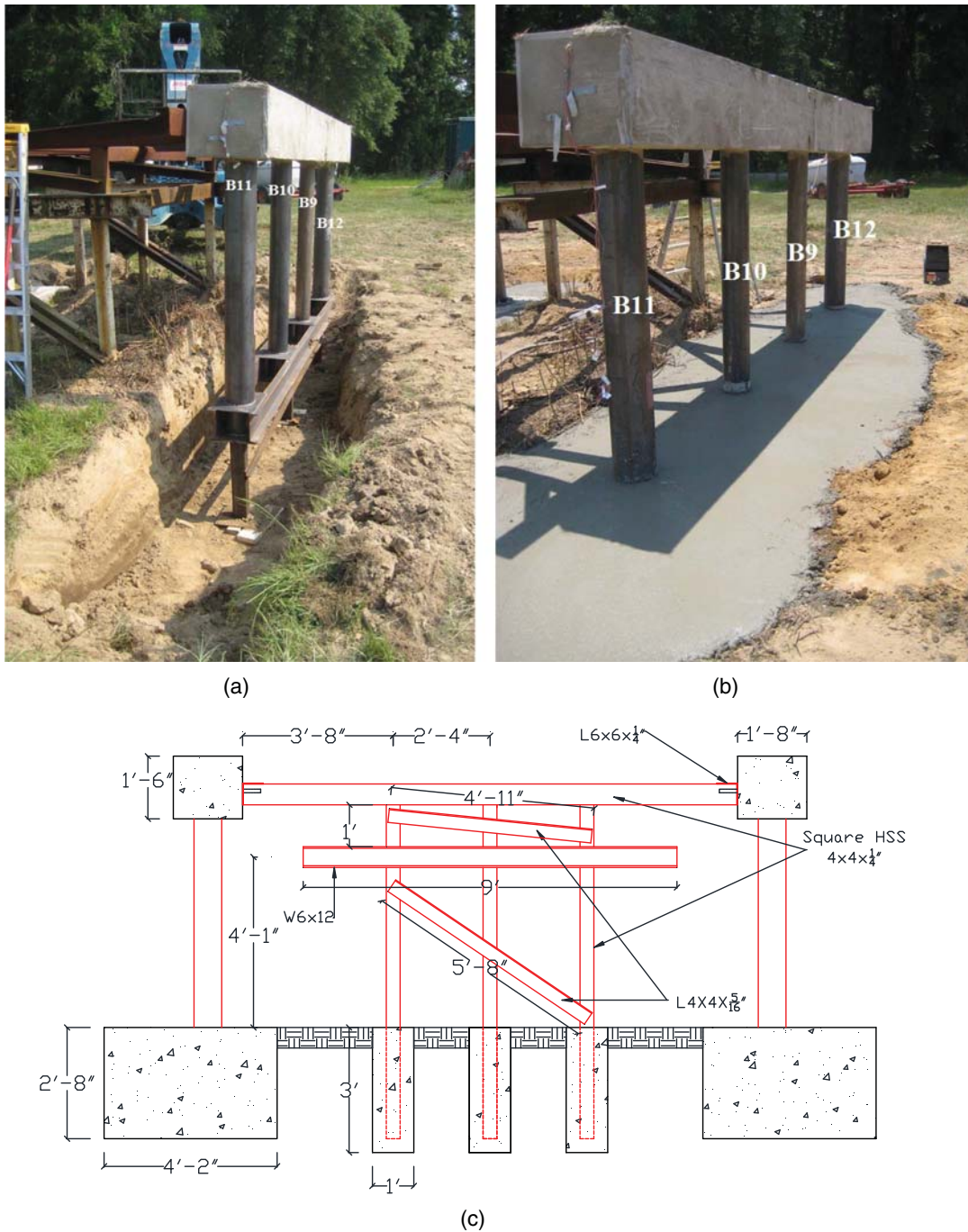


**Fig. 5.** Reaction frame elevation and attached bents: (a) typical bent set in place; (b) same bent after footing has been poured; (c) schematic side view of test setup (units shown in feet and inches, 1 in. = 25.4 mm)

1,270 mm (50 in.) on center for the columns of each bent would amply suffice for that purpose. A reaction frame [Fig. 5(c)] connected to the cap beam of each bent served to provide lateral support and simulate the boundary conditions and rigidity that the deck of a bridge would have provided at the top of the beams if it were present. Information on the design of the cap beam, the foundation, and the construction sequence is provided in Fouché and Bruneau (2014).

## Instrumentation

For the cyclic tests, the instrumentation was designed to capture primarily the force-displacement response of the specimens, such as to characterize ductility and hysteretic behavior of such sections. To get redundancy in the main measurements, three different measurements of specimen deformations were taken: from the displacement transducer in the actuator (which also recorded deformations of the reaction frame), from a set of string displacement potentiometers (string pots) connected to an external reference point, and from a Krypton Dynamic Measurement Machine (model K600 by Nikon Metrology). Fig. 6 shows a close up view of a specimen and the locations of some of the instruments. Drawings with precise locations of instruments are in Fouché and Bruneau (2014).

For the blast tests, because of issues related to survivability of instruments in the fireball, instrumentation of the specimen for the *ECLIPSE* tests was kept simple and primarily consisted of two quartz free-field ICP blast pressure pencil probes and a high-speed camera. The instrumentation scheme for the ERDC test series was designed with the intent to collect more information than was obtained in the *ECLIPSE* test series. To obtain information on the peak velocity of the specimen during its response and to estimate the impulse seen, a series of shorting pins was used. However, the use of shorting pins was more successful in tests conducted shortly thereafter on a different type of column, because more pins were used in those tests than for the CFDST columns described here [see Fouché et al. (2016) for a description of the shorting pins concept and example results]. In addition, overpressures were measured for all tests using a pencil pressure probe placed at a fixed standoff of

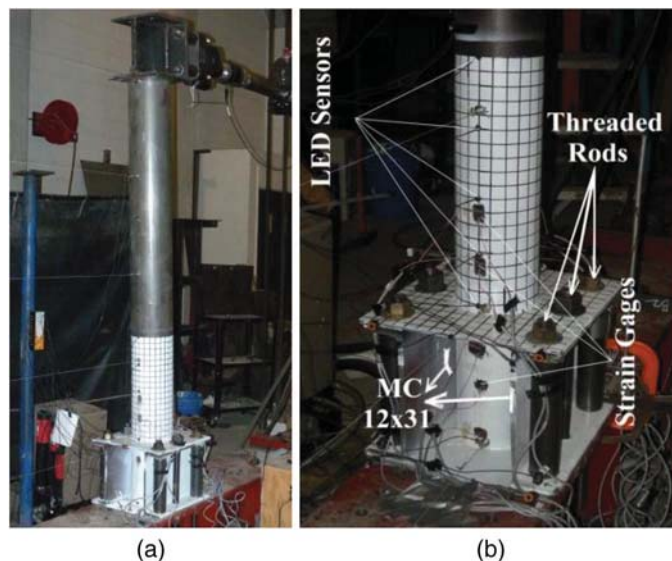


**Fig. 6.** Typical cyclic test specimen setup: (a) global view; (b) close up showing partial instrumentation

94x, where 1.0x corresponds to a standoff distance (measured in ft or m) that corresponds to a severe threat having a scaled distance of  $0.12 \text{ m/kg}^{1/3}$  ( $0.30 \text{ ft/lb}^{1/3}$ ). The term *scaled distance* corresponds to the standoff distance, or just *standoff*, (measured in ft or m) divided by the cube root of the charge weight (lb or kg). The scaled standoff (measured in ft or m) is simply the standoff distance multiplied by a factor. In conducting scaled experiments when the cube root scaled distance is maintained (following Hopkinson-Cranz scaling) then the peak blast pressures will scale appropriately (1:1). Properly scaling the pressure-impulse is achieved by the dimensional scaling of the test item. Attempts were made to record acceleration histories at the back of the specimens by using shock accelerometers of 200,000 and 60,000 g capacities, but this did not yield satisfactory results, because capacities of the accelerometers were exceeded during the tests.

## Experimental Protocol

### Cyclic Tests

During the experiments, the specimens were subjected to a conventional cyclic pushover test during which each specimen was subjected to cyclic displacements of progressively increasing amplitudes up to failure. At each specified displacement cyclic amplitude, the specimen was subjected to at least three cycles. Each specimen underwent a total of at least 30 cycles with the total number of cycles applied before failure varying, depending on each specimen's ductility. All tests were conducted in displacement-control mode. In the initial stage of loading, the increments in displacement were smaller to capture each specimen's first yielding and to use the resulting yield value to define the subsequent cycles (because the loading protocol is in terms of multiples of the yield displacement). Once the yield displacement was determined, the full loading displacement history was followed. Note that because the CFDSTs were tested to ascertain their potential for use as bridge columns that sustain a relatively modest axial load (less than 10% of its axial strength), no axial force was applied to the columns. Only the lateral-displacement history presented for the test protocol was applied at the top of the specimens. Note that testing continued until little residual strength remained to allow quantifying the rate of strength degradation that would be needed to be able to perform analytical studies such as those described in FEMA 356 (FEMA 2000) or FEMA 695 (FEMA 2009) (although such analyses are not part of the current scope of work). To facilitate the visualization of local deformation in the specimens, the bases of all specimens (except for S4) were coated with white wash, and a grid was drawn over the base of the specimen (Fig. 6).

### Blast Tests

The charge weight was chosen to be consistent with a design threat based on a scenario in which a vehicle borne improvised explosive device (VBIED) is detonated near a column of the corresponding full-scale bridge. Charges and charge distances were chosen to provide example results for three limit states: (1) to create plastic deformations in the specimens to ascertain how they deform globally and locally under blast loading; (2) to induce the maximum feasible deformation without compromising stability of the column specimens under axial load; and (3) to bring the specimen to the point of incipient collapse to determine the likely failure mechanism. Note that for all specimens, the center of gravity of the charges was 25.4 cm (10 in.) above ground.

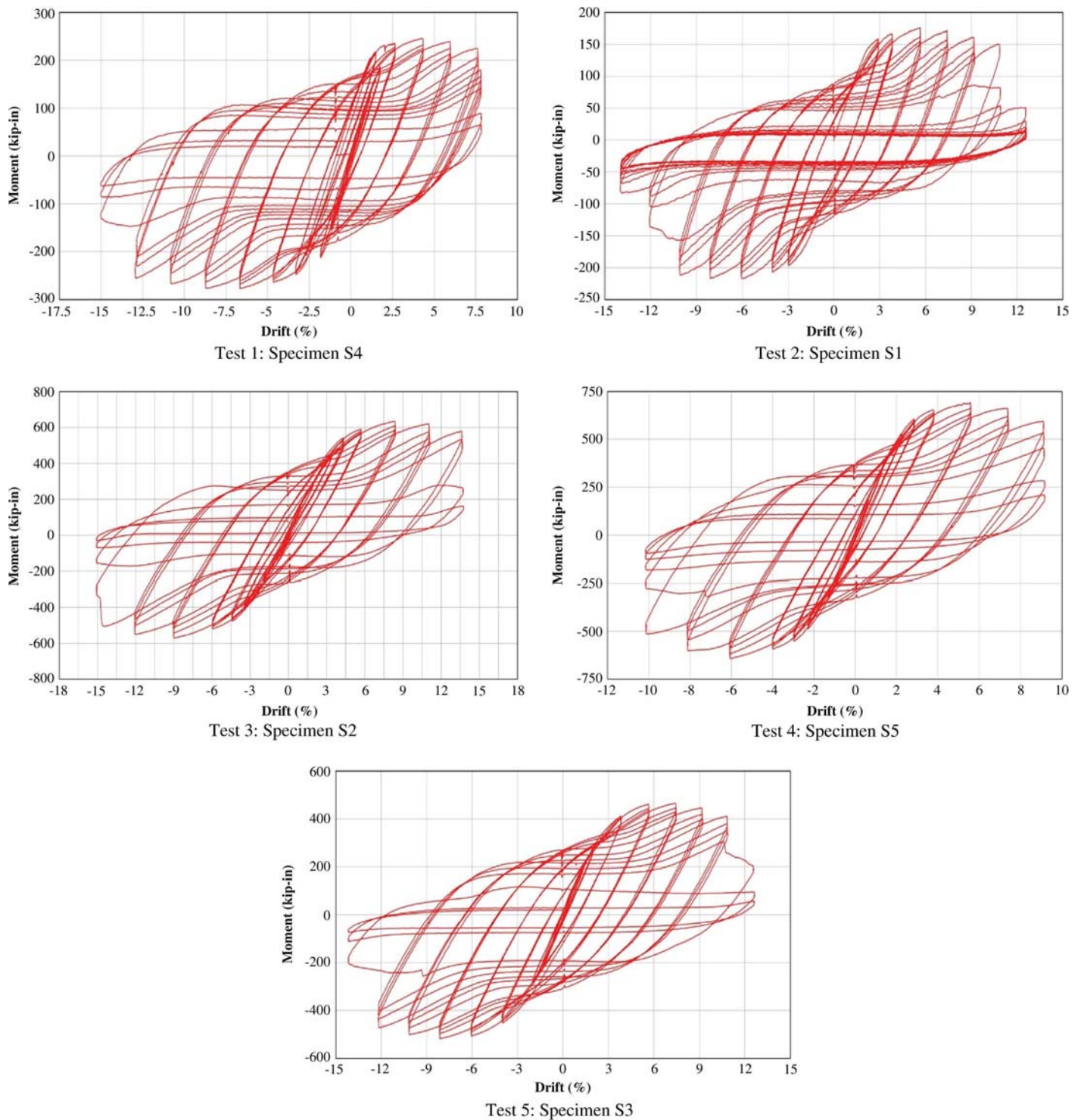


**Fig. 7.** Hysteresis loops for the specimens tested

### Experimental Results: Cyclic Tests

The force displacement curves obtained for all specimens are shown in Fig. 7. Descriptions of observed behavior and its effect on the hysteretic results follows for each tested specimen.

#### Test 1: Specimen S4

When the specimen was cycled at stroke amplitudes of 50 mm (2 in.), it was observed that the load displacement curve departed from a straight line at an actuator stroke of 38 mm (1.5 in.).

The displacement measured by the linear potentiometer at this time was 23 mm (0.90 in.), which corresponded to a drift of 1.3%. When yielding occurred, the applied force was 12.2 kN (2.75 kips). Based on the deformation measured by the linear potentiometer, the corresponding stiffness was 0.37 kN/mm (2.12 kip/in.). The specimen did not reach its maximum lateral strength of 18.3 kN (4.12 kips) [moment strength of 31,320 kN-mm (277.1 kip-in.)] until reaching a drift of 6.65%.

At a drift of 4.3%, a buckling wave started to grow at the base of the specimen. The lateral strength of the specimen at the time was

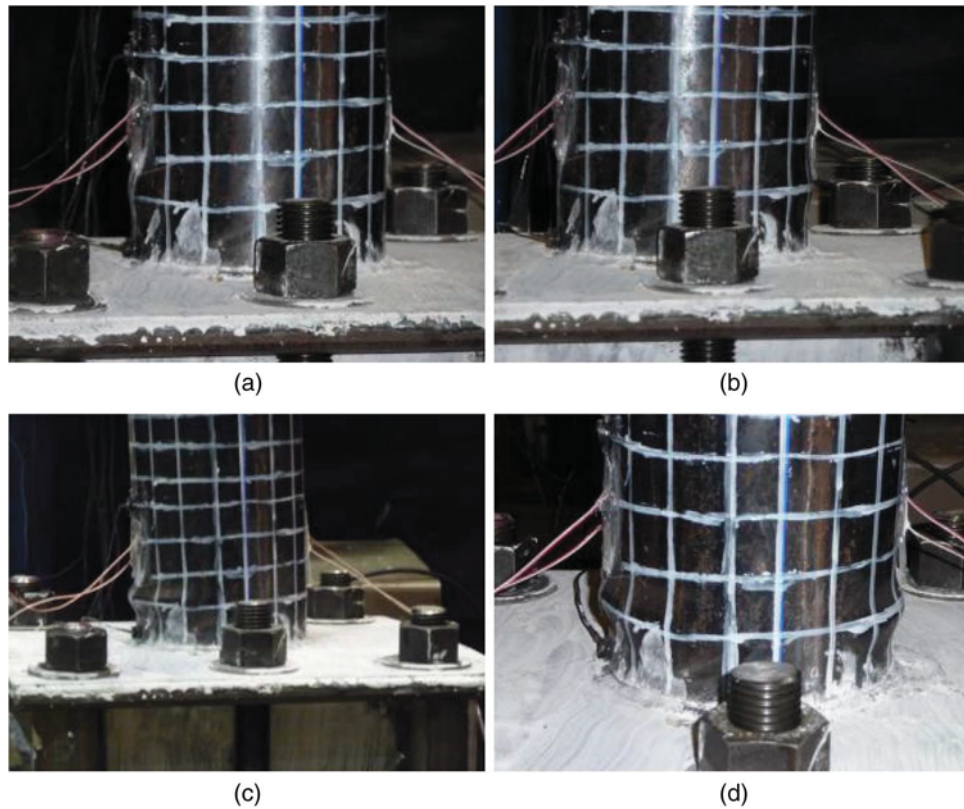


**Fig. 8.** Buckling progression of S4

16.2 kN (3.65 kips). Those buckling waves observed at 4.3% drift kept growing on the outside tube from cycle to cycle. At a drift of 7.8%, they reached a peak wavelength of approximately 25 mm (1 in.), with a peak amplitude of 19 mm (3/4 in.) on the most compressed side of the specimen. At this stage, the bulges grew to encompass approximately half of the circumference of the outside tube (Fig. 8).

When the drift reached 7.8%, the actuator ran out of stroke on one side. It was decided to keep cycling the specimen at unequal displacement amplitudes. The amplitude of the displacement on the actuator side kept increasing, whereas it remained fixed at a maximum amplitude of 7.8% drift in the other direction. On the 3rd cycle at a drift of 13% on the actuator side, localized necking in the buckled region on the outside tube was noticeable in the steel. A crack appeared in that region during the next cycles (at 15% drift), followed by almost a 50% drop in strength. Pulverized concrete spilled out of the crack (Fig. 9). It was decided to continue the

test to see whether the inside tube would easily fracture. After three cycles at 15% drift on the actuator side, the inner tube had not ruptured; the test was stopped when the drop in strength was approximately 80% of the maximum value reached during the test. This is equal to the strength (5,760 kN-mm, 51 kip-in.) of the composite section formed by the concrete and the inner tube acting as a dowel. This also indicates that the outside tube, although not participating in the resistance of the section per se, was still confining the concrete core.

#### **Test 2: Specimen S1**

To prevent the actuator from running out of stroke in one direction, as in the previous case, a spacer was added between the specimen and the reaction frame to allow development of the full travel length of the actuator in both directions. Departure from elastic behavior was observed for the specimen at a stroke of 38 mm (1.5 in.), which



**Fig. 9.** Failure of S4

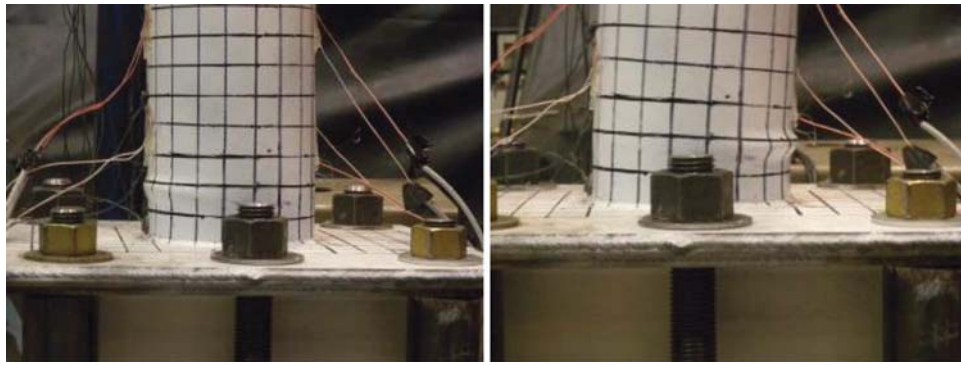


**Fig. 10.** First buckling of Specimen S1

corresponded to a measured deformation of the specimen of 23 mm (0.9 in.) or 1.3% drift. The strength at yield was 7.9 kN (1.78 kips), and the apparent lateral stiffness was 0.35 kN/mm (1.98 kip/in.).

A visible local buckle started to grow on the side opposite the actuator when the specimen was cycled at 3.8% drift. This buckle was located 51 mm (2 in.) from the top plate of the base connection; its wavelength was approximately 13 mm (0.5 in.), and its amplitude was 19 mm (3/4 in.) (Fig. 10). The occurrence of buckling in the specimen was directly followed by pinching in the force-displacement curve. By a drift of 5.4%, the buckling wave was fully formed. At the same time, the specimen reached its maximum strength of 14.4 kN (3.23 kips) [moment strength of 25,550 kN-mm [217.2 kip-in.)].

By 7.3% drift, a crack on the side opposite the actuator became visible [Fig. 11(a)]. This was directly followed by another crack on the actuator side of the specimen when the load was reversed,

which corresponded to a 33% reduction in strength. As the crack grew, the specimen gradually lost strength. Fracture of the specimen occurred during this same cycle [Fig. 11(c)], and pulverized concrete came out of the crack. As the specimen was further cycled, the hysteresis loop of the specimen stabilized to a residual loop. The residual loop was not symmetric; the average of the negative and positive peak forces was 3,220 kN-mm (28.5 kip-in.), which is close to the capacity of the inner tube (3,208 kN-mm, or 28.4 kip-in.).

### **Test 3: Specimen S2**

Yielding occurred at a stroke of 38 mm (1.5 in.); the corresponding potentiometer measurement was 23 mm (0.9 in.), the yield force was 26 kN (5.85 kips), and the apparent stiffness was 1.14 kN/mm (6.5 kip/in.). Although some pinching in the hysteric curve was

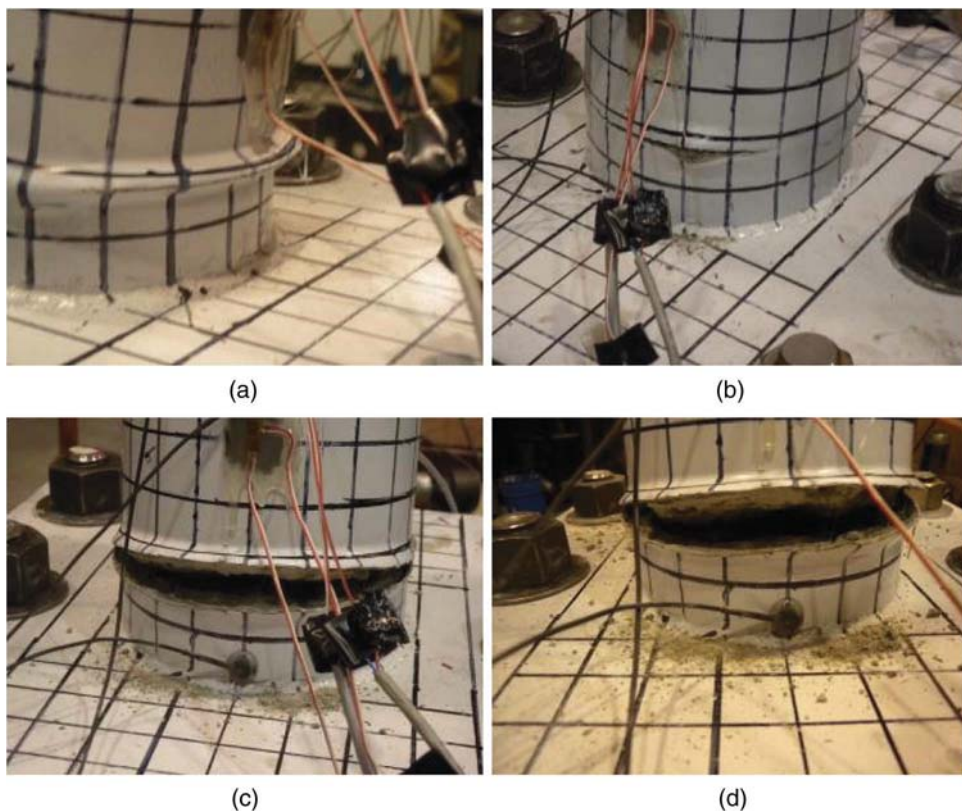


**Fig. 11.** Progression of failure in S1

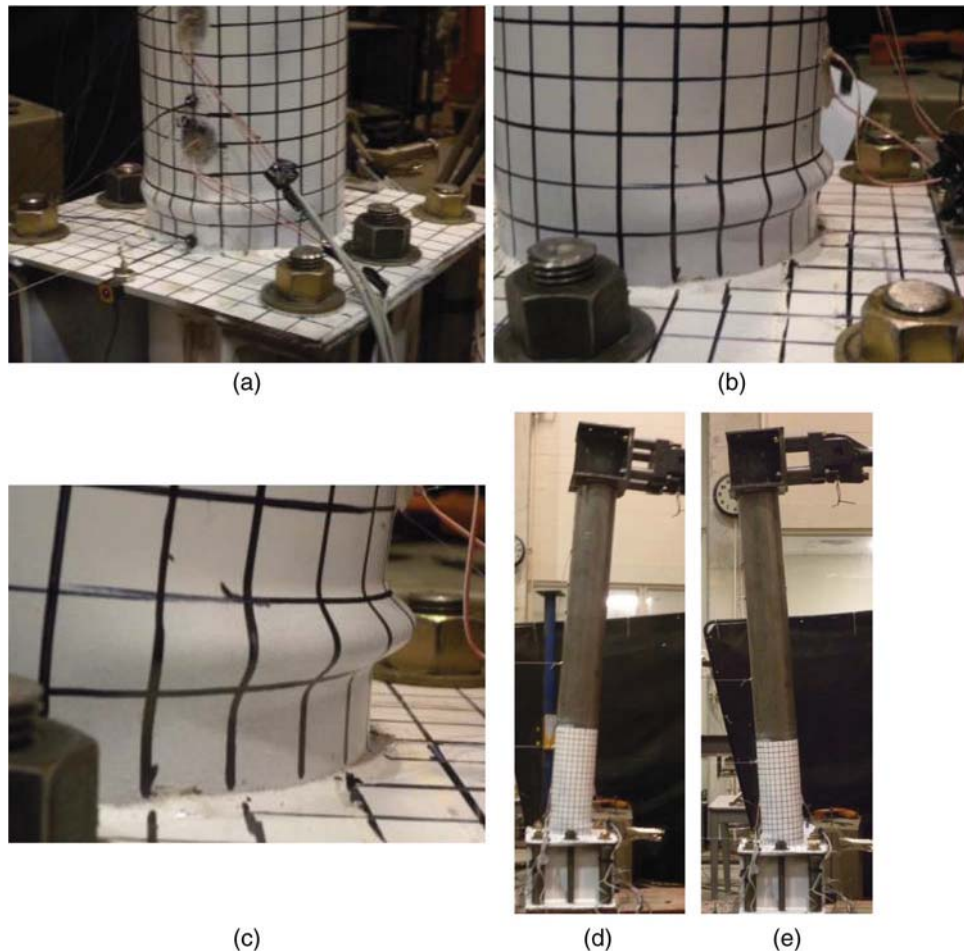


**Fig. 12.** Specimen S2: (a–c) progression of buckling; (d and e) deflected shape at 5.7% drift

already visible in the force-displacement at a drift of 5.7%, the first buckling wave did not really form until the specimen reached its peak lateral strength of 42 kN (9.44 kips) (moment capacity of 71,760 kN-mm, or 634.84 kip-in.), at a drift of 8.4% on the side opposite the actuator. From there, the buckle grew to its final amplitude of approximately 25 mm (1 in.) at 11% drift; its wavelength was about the same (Fig. 12).

Necking of the steel toward the fixed base of the specimen was detected on the tension side during the first cycle at 13.6% drift. On load reversal, a crack formed suddenly in the previously compressed side. The strength of the specimen was reduced by approximately a third.

The specimen was cycled at that amplitude to assess the residual strength provided by the inner tube as was done in the previous tests. The average residual moment strength (25 kip-in.) was approximately equal to the inner tube capacity (22.24 kip-in.).

#### **Test 4: Specimen S5**

Yielding of the specimen occurred at the same stroke of 38 mm (1.5 in.) (0.9-in. specimen displacement or 1.3% drift) for an applied force of 20 kN (7 kips), which resulted in an apparent stiffness of 1.4 kN/mm (7.8 kip/in.). The lateral strength of the specimen reached a maximum of 45.8 kN (10.3 kips) [moment strength of 78,230 kN-mm (692.7 kip-in.)]. Buckling occurred at a drift of 5.7%. The maximum strength was also reached at this drift, as consistently observed for the other specimens.

On the side opposite to the buckle, the coating applied to the specimen started to flake, indicating that S5 was further yielding. At 7.4% drift, a buckle *bulge* grew to encompass the entire diameter of the specimen; the crest of that bulge was approximately 19 mm (0.75 in.) more than a wavelength of 25 mm (1 in.). Flaking of the coating intensified as a sign of further plasticization.

Fracture in the buckled region was visible during the cycles at 9.1% drift. Deformation of the base of the specimen until failure progressed similarly to the behavior observed in all other specimens. At rupture, the residual strength of the specimen was approximately 9,000 kN-mm (80 kip-in.), which is higher than the resistance of the inner tube of itself at 7,267 kN-mm (64.35 kip-in.). This suggests that some concrete was still contributing to that residual strength; as a matter of fact, the specimen was not cycled up to the point beyond fracture, after which stable residual loop could be observed (as in the other specimens).

#### **Test 5: Specimen S3**

Yielding of the specimen was observed at approximately 1.3% drift (23 mm, 0.9 in. measured by the potentiometer). At yield, the lateral strength of the specimen was 16.9 kN (3.8 kips), and its apparent stiffness was 0.74 kN/mm (4.2 kip/in.). S3 did not show any sign of local buckling until a drift of 8.1%. First visible evidence of local buckling occurred when the specimen attained its peak lateral strength of 32.5 kN (7.3 kips), with corresponding

moment strength of 58,470 kN-mm (517.3 kip-in.), which was consistent with the previous observations. The buckling wave spanned the full diameter of the specimen; its amplitude was 13 mm (0.5 in.), and its wavelength was 25 mm (1 in.). The strength of the specimen degraded significantly when the drift reached 12.2% when the specimen suddenly lost 50% of its strength. This drastic reduction in strength was attributable to crack initiation in the buckled region at the apex of the buckling wave.

### Summary of Findings: Cyclic Tests

All the specimens that were part of this quasi-static test program and that were conducted to assess the seismic resistance of CFDSTs exhibited ductile behavior up to failure. For all specimens, irrespective of void ratio, yielding of the section preceded buckling of the outside tube; this was expected, because all the tubes were compact. Yielding of the specimens did not occur until the actuator applied a displacement of 38 mm (1.5 in.), corresponding to a drift of 1.3%. Local buckling of the outside tube was not observed until well beyond 4% drift. Failure of all the sections happened generally beyond 7%, even when compactness of the outside tube met only the AISC 341-10 (AISC 2010) requirements for moderately ductile behavior.

Once a specimen reached its peak strength, no substantial reduction in strength was observed for the specimen prior to development of fracture in the outside tube. Also, the loss in effective stiffness (ratio of peak strength to applied displacement at any given cycle) for all specimens was gradual. Although pinching of the hysteresis curve proportional to the severity of local buckling happened during the tests, the curve was stable, showing that the energy dissipation capacity of this specimen would have been fairly reliable under earthquake excitations.

Specimens S2 and S5 had similar strengths, but the void ratio of S5 was more than twice that of S2. Both used moderately ductile tubes on the inside. Both specimens reached similar deformation and strength levels; however, the residual hysteresis for S5 showed higher strength owing to the fact that the inner tube of S5 had higher strength than that of S2. Thus, S5 would offer better protection than S2 under cyclic loading, which is significant if a CFDST with a higher void ratio involves cost-saving.

### Experimental Results: Blast Tests

Cross-section deformation (denting/caving) was an important deformation mechanism for CFDSTs subjected to overpressures from a near-contact explosion; global deformations are thus reported in two formats. For sections that were not dented, maximum lateral bending deformation and the associated rotations at three locations (top, bottom, and point of maximum deformation) are reported. For dented sections, the maximum lateral deformation and cross-section deformations are reported. The maximum lateral deformation in that case includes the dent depth and needs to be corrected for denting so that rotation attributable to bending only can be calculated.

#### Tests 1–4: Specimens B8, B2, B4, and B6

As indicated in Table 6, Specimens B8, B2, B4, and B6 were, respectively, subjected to a charge  $W$  at scaled standoff distances of 1.71 $x$ , 2.29 $x$ , 1.43 $x$ , and 2.29 $x$  (recall that 1.0 $x$  is for a standoff distance that corresponds to a scaled distance of 0.12 m·kg<sup>1/3</sup> (0.30 ft·lb<sup>1/3</sup>). These were higher standoff distances than for all subsequent tests. The values of  $W$  and  $x$  are kept confidential for security purposes, as commonly done for this type of experiment. Recall that the distance between columns in the bents was designed such that the blast test on any target column had no impact on the adjacent columns (also benefiting from results from similar tests on CFST and reinforced concrete columns in tests by Fujikura et al. (2008) and Fujikura and Bruneau (2011).

Specimen B8 was a CFST (i.e., no void) whose purpose was to provide a point of comparison with previous tests reported on CFSTs and CFDSTs of similar strength, whereas B2, B4, and B6 had the relatively smaller void ratios of 0.38, 0.42, and 0.25. B8 had a measured average outside diameter of 150.6 mm (5.93 in.) and a measured wall thickness of 3 mm (0.120 in., nominal 0.125 in.); this resulted in compactness in compliance with the limit for highly ductile members (per AISC 341). The maximum deformation measured for this test occurred at a height of 406.4 mm (16 in.) from the top of the foundation and was approximately 25.4 mm (1 in.). This corresponds, respectively, to overall rotations of 0.063 rad at the base of the specimen and 0.024 rad at the top of the specimen, resulting in a 0.087 rad in-span rotation. A sense for the global

**Table 6.** Results for the Blast Tests

Test	Column tested	Void ratio	Scaled standoff	Maximum deformation [mm (in.)]	Height of maximum deformation [mm (in.)]	$B$ [mm (in.)]	$D$ [mm (in.)]
1	B8	0	1.71 $x$	25.4 (1)	406 (16)	—	—
2	B2	0.42	2.29 $x$	19 (3/4)	254 (10)	—	—
3	B4	0.38	1.43 $x$	17.5 (11/16)	254 (10)	—	—
4	B6	0.25	2.29 $x$	12.5 (1/2)	254 (10)	—	—
5	B7	0.63	1.29 $x$	116 (4.56)	254 (10)	121 (4.75)	229 (9)
6	B5	0.33	1.29 $x$	76 (3)	254 (10)	132 (5.2)	165 (6.5)
7	B1	0.33	1.29 $x$	111 (4.4)	305 (12)	124 (4.9)	165 (6.5)
8	B3	0.50	1.00 $x$	73 (2.88)	305 (12)	178 (7)	165 (6.5)
9	B8	0	1.00 $x$	Failed	—	—	—
10	B2	0.42	1.29 $x$	135 (5.25)	381 (15)	123 (4.82)	175 (6.9)
11	B6	0.50	1.07 $x$	175 (6.88)	356 (14)	145 (5.7)	248 (9.8)
12	B4	0.38	1.07 $x$	127 (5)	356 (14)	130 (5.12)	191 (7.5)
13	B9	0.42	1.29 $x$	114 (4.5)	305 (12)	114 (4.5)	173 (6.82)
14	B10	0.38	1.29 $x$	76 (3)	254 (10)	(5.38)	187 (7.38)
15	B11	0.50	1.71 $x$	37.5 (1.48)	254 (10)	172 (6.72)	211 (8.3)
16	B11	0.50	1.43 $x$	119 (4.7)	254 (10)	121 (4.75)	187 (7.38)
17	B12	0.62	1.29 $x$	127 (5)	254 (10)	—	—

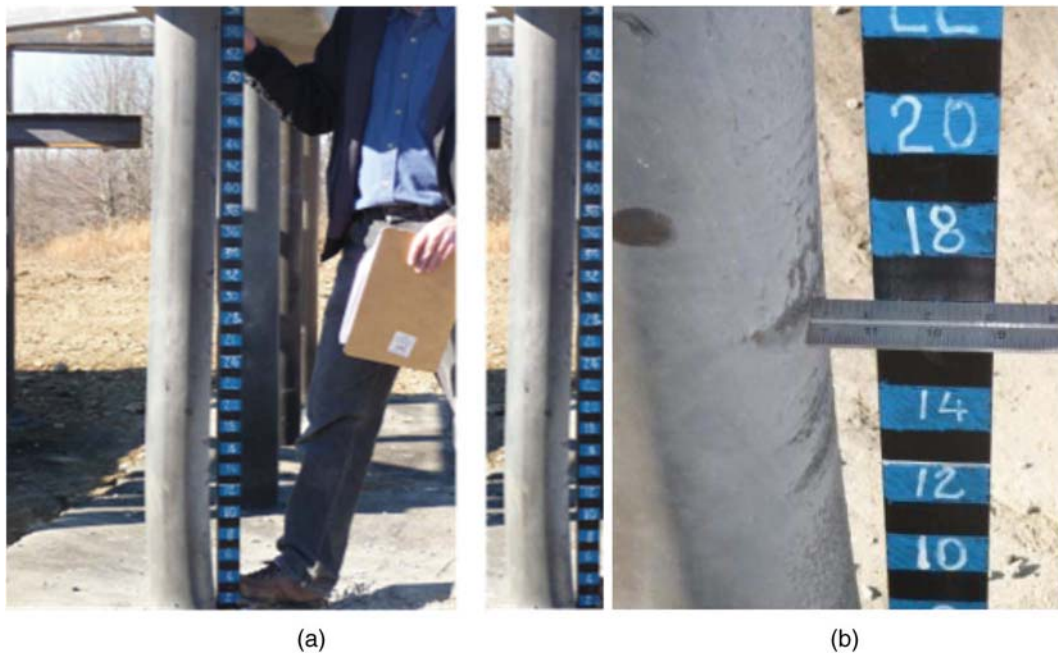


**Fig. 13.** Deformation along the height of Specimen B8, as a representative global deformation: (a) distribution along the height; (b) maximum deformation

distribution of deformations along the height of B8 can be gathered from Fig. 13(a), whereas Fig. 13(b) shows a crude measurement of the maximum deformation of B8 using a ruler.

For Specimen B2, the diameter-to-thickness ratios of the inner and outer shells complied with the limits for highly ductile and moderately ductile members as per AISC 341 (AISC 2010). In comparison to B8, B2 had a lower expected strength. Consequently, it was tested at a scaled standoff of  $2.29x$ . The maximum measured plastic deformation for this test was 19 mm (3/4 in.) measured at 254 mm (10 in.) from the base of the specimen. The corresponding calculated rotations at the bottom and top of that specimen were, respectively, 0.075 and 0.016 rad. The in-span rotation necessary to achieve those rotations at the top and the bottom is 0.091 rad.

The inner and outer tubes of B4 were chosen to have highly ductile behavior. A maximum deformation of 17.5 mm (11/16 in.) for Specimen B4 was observed at 254 mm (10 in.) from the ground. The angles of rotations at the base and the top of Specimen B4 were calculated to be 0.069 and 0.014 rad, respectively. These combined for an in-span rotation of 0.083 rad.

Designed with tubes expected to have highly ductile behavior (inner tube) and moderately ductile behavior (outer tube), Specimen B6 had also the smallest void ratio (25%) of all the specimens tested. B6 had similar predicted strength to B4. The scaled standoff for the test on B6 was set at  $2.29x$ . At the end of the test, the maximum measured deformation of B6 was 12.5 mm (1/2 in.) at 254 mm (10 in.) from the ground, which corresponded to a base rotation of 0.05 rad and a top rotation of 0.01 rad. The in-span rotation for that case was 0.06 rad. In all four tests, the cross section of the specimens remained circular; no significant deformation was observed between the pre- and postshot measurements of the cross section.

### Tests 5–7: Specimens B7, B5, and B1

All three specimens were tests at a scaled standoff of  $1.29x$ . Specimen B7 had comparable strength to B3, the strongest specimen, but had the biggest void ratio and the thinnest composite wall at

37.5 mm (1.5 in.) of all the specimens. Both inner and outer tubes of B7 were expected to exhibit highly ductile behavior. After the test, local denting of the cross sections of the specimen was observed over a region extending approximately 460 mm (18 in.) from the base of the specimen [Fig. 14(a)]. This is approximately twice the height of burst. The valley of the dent was the maximum

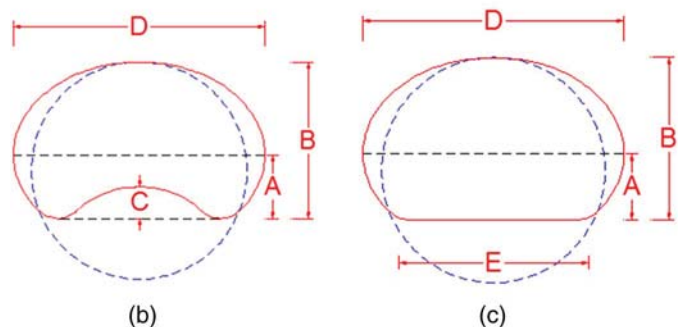
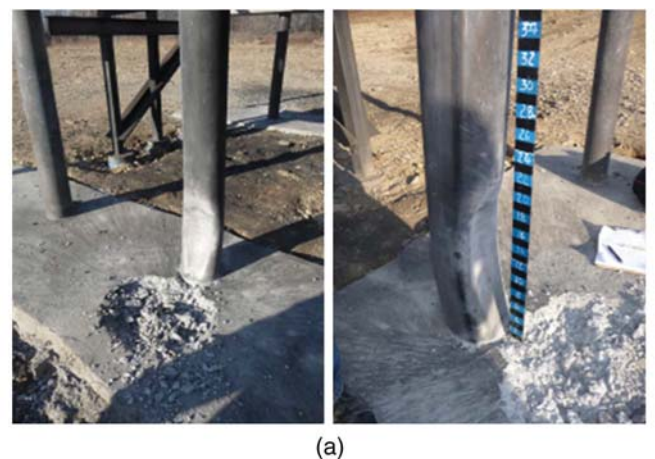


**Fig. 14.** Overview of the deformations of Specimen B7

**Table 7.** Cross-Section Deformations of B7

<i>H</i> [mm (in.)]	<i>B</i> [mm (in.)]	<i>C</i> [mm (in.)]	<i>D</i> [mm (in.)]
457 (18)	133 (5.25)	N/A	222 (8.75)
356 (14)	127 (5.00)	22 (0.88)	229 (9.00)
305 (12)	127 (5.00)	25 (1.00)	229 (9.00)
254 (10)	123 (4.75)	32 (1.25)	N/A
203 (8)	123 (4.75)	19 (0.75)	225 (8.88)
152 (6)	116 (4.56)	16 (0.63)	225 (8.88)
102 (4)	121 (4.75)	6 (0.25)	N/A

at a height of 254 mm (10 in.) from the top of the foundation. The profile of the dent was measured, and its main dimensions are reported in Table 7 for the dented shape schematically shown in Fig. 14(b).

The total lateral deformation of the specimen (including denting) at the same location corresponded to the maximum observed deformation of the test and was measured to be 116 mm (4.56 in.). A crack 97 mm (3.8 in.) long and 12.5 mm (0.50 in.) wide was also observed in the outside tube at 43 cm (17 in.) from the base of the specimen (Fig. 15).

After removal of the concrete of the foundation, further observations and measurements on the specimen were conducted. In particular, another crack was noted at the junction between the specimen and the top plate of the foundation beam (Fig. 16). Also, the dented region extended all the way down to that junction.

**Fig. 15.** Crack in Specimen B7**Fig. 16.** Crack in Specimen B7 in the outside tube at the specimen to foundation beam connection**Table 8.** Cross-Section Deformations of Specimen B5

<i>H</i> [mm (in.)]	<i>B</i> [mm (in.)]	<i>D</i> [mm (in.)]	<i>E</i> [mm (in.)]
508 (20)	149 (5.88)	156 (6.13)	99 (3.9)
406 (16)	140 (5.50)	159 (6.25)	99 (3.9)
317 (12)	133 (5.25)	166 (6.50)	99 (3.9)
203 (8)	133 (5.25)	166 (6.50)	99 (3.9)
102 (4)	143 (5.63)	168 (6.63)	99 (3.9)
51 (2)	N/A	N/A	99 (3.9)

Specimen B5 had an overall void ratio of 33%, and both tubes in the cross section were expected to behave in a highly ductile manner. The thickness of the composite wall for this specimen was 50 mm (2 in.). After the test, B5 had a maximum residual deformation of 76 mm (3 in.) at 254 mm (10 in.) from the ground. Some flattening of the face of the specimen exposed to the blast was noted, and the overall section at that location deformed into an oval shape with small and big axes' measures of 132 mm (5.2 in.) and 165 mm (6.5 in.), respectively. The profile of the dent was measured, and its main dimensions are reported in Table 8 for the deformed shape schematically shown in Fig. 14(c).

Similar to B5, B1 had a void ratio of 33%, but its inner tube was expected to behave in a highly ductile manner—with moderately ductile for the outside tube. This specimen design swapped the thicknesses of the tubes used to fabricate B5, whereas the diameters of the tubes were kept the same. The predicted strengths of the specimen differed by less than 10%. However, this specimen was expected to be more flexible. Because of that similarity in strength, the standoff was kept the same as for B5. The posttest permanent deformation of 111 mm (4.4 in.) was measured at the location of maximum deformation at 305 mm (12 in.) from the base (Fig. 17). As for Specimen B5, the front face of the specimen flattened into an oval shape with measured axes of 124 mm (4.9 in.) and 165 mm (6.5 in.) in the region of maximum deformation. Note that those deformations are fairly similar to the ones recorded for B5 attributable to the similar design features between the two specimens. The front face of the specimen appeared wrinkled in the flattened area, and at least five visible lobes formed over that face. After removal of the cover concrete of the base, a fracture at the connection

**Fig. 17.** View of the global deformation of Specimen B1



Fig. 18. Final deformed shape of Specimen B2



Fig. 19. Fracture at the base of Specimen B2

of the specimen to the top plate of the foundation beam was found. This fracture, combined with the partial removal of the cover concrete of the foundation near the base of the specimen, might have contributed to the measured deformation.

#### Tests 8–9: Specimens B3 and B8

Both specimens were tested at a scale standoff of 1.00x, the closest of all the series. Specimen B3 had the second largest void ratio

(50%) after B7 and largest strength. The maximum deformation of B3 was 73 mm (2.88 in.), measured at a height of 305 mm (12 in.) from the top of the footing.

A piece approximately 305 mm (12 in.) long sheared off the base of Specimen B8, whereas the rest was torn out from the underside plate of the cap beam at the location it was attached. The piece sheared from the base was found approximately 30 m (100 ft) from the test setup. Its location was also offset from the test setup. The offset angle was estimated to be 30 degrees. Note that the same failure mode was observed by Fujikura and Bruneau (2011) in their previous tests on CFST. The rest of the specimen was found on the ground.

#### Tests 10–12: Specimens B2, B6, and B4

Specimen B2 was retested at a closer scaled standoff (1.29x) than the first time. Specimens B6 and B8 were tested at a scaled standoff of 1.07x.

After the second test, the concrete covers of the cap and foundation beam in the vicinity of B2 were removed. The overall deformation of the test, including the residual deformation from the previous test, was 135 mm (5.25 in.) at 381 mm (15 in.) from the top of the foundation beam. Significant denting of the section accompanied this deformation, with a  $C$  value of [parameter schematically shown in Fig. 14(b)] 21 mm (0.83 in.). The final deformed shape of Specimen B2 is shown on Fig. 18. Fracture of the outside tube occurred (Fig. 19), but as mentioned in the test objective, this was expected. Note that the inside tube did not fracture. In this design, the inner tube provided a dowel action that prevented the specimen from shearing away (as happened to the previous test on Specimen B8) in spite of the fracture of the outside tube.

Specimen B6 was tested a second time. An important indentation was observed in B6 posttest. The maximum final deformation of B6 was 175 mm (6.88 in.) at 356 mm (14 in.) from the top of the foundation. This represented an additional 162.5 mm (6.38 in.) of deformation over those measured in Test 4. The final deformed shape of the specimen is shown Fig. 20. The cross section was also severely dented with a measured  $C$  value of 15.4 mm (0.6 in.).

#### Test 12 Specimen B4

The second test on Specimen B4 was conducted at a scaled standoff of 1.07x. The maximum deformation of B4 was measured to be 127 mm (5 in.) at a height of 356 mm (14 in.) over the top of the footing. The tube was indented over most of the region extending approximately 510 mm (20 in.) from the top of the foundation. The indentation was the deepest at the point at which the maximum lateral deformation of the element was measured. The average



Fig. 20. Denting and fracture of Specimen B6



**Fig. 21.** Observed deformation of Specimen B9 (images by P. Fouché)

minor and major axes of the deformed cross section at the location of maximum lateral deformation for B4 measured, respectively, 130 and 191 mm (5.12 and 7.50 in.). Fracture of the outside shell of B4 occurred above the weld connecting the specimen to the top of the embedded foundation beam.

### Test 13: Specimen B9

This test provided additional data on the behavior under the blast of CFDST falling near the median for the range of void ratios tested. The same charge weight and standoff as in Test 10 were maintained (but B9 was tested only once, contrary to B2). The maximum measured deformation on the front side of the specimen was 114 mm (4.50 in.) at 305 mm (12 in.) from the top of the foundation. Although more accurate measurements were made using a digital Vernier caliper, Fig. 21 shows an ad-hoc measurement made on the specimen using two measuring tapes. As previously observed, a region extending approximately 457 mm (18 in.) from the top of the foundation was dented with a maximum C value of 11.1 mm (7/16 in.); the indentation reached its greatest depth at the point where the maximum lateral deformation of the specimen was measured. The dent profile was measured by using the depth probe of a

Vernier caliper at different stations along the dented region (Table 9).

### Test 14: Specimen B10

Specimen B10, a replica of Specimen B4, was highly ductile and had a void ratio of 42%. A smaller standoff of 1.29x was used for this test, compared with 1.43x for B4. The same trend in response was observed with a combination of denting and bending of the specimen. The dented region was similar to that observed for the previous specimen. The indentation on that specimen reached a maximum C value of 11.1 mm (7/16 in.), although the void was slightly bigger than for B9 (0.42 versus 0.38%). The maximum measured deformation of Specimen B10 was 76 mm (3 in.) at 254 mm (10 in.) from the top of the foundation. Deformations of the cross-section level along the base of the specimen are reported in Table 9.

### Test 15: Specimen B11

Specimen B11 had a void ratio of 50% with the same nominal tubes diameters as B6; however, the thickness of the outer tube was increased to improve the ductility of the outside tube. Specimen B11

**Table 9.** Cross-Section Deformations in Specimens B9 and B10

H [mm (in.)]	B9 [mm (in.)]				B10 [mm (in.)]		
	A	B	C	D	B	C	D
508 (20)	N/A	N/A	0.00	159 (6.25)	N/A	N/A	N/A
457 (18)	64 (2.50)	133 (5.25)	0.00	165 (6.50)	162 (6.00)	0.0	165 (6.50)
406 (16)	60 (2.38)	127 (5.00)	2 (0.06)	168 (6.63)	146 (5.75)	0.0	165 (6.50)
381 (14)	54 (2.13)	121 (4.75)	3 (0.13)	173 (6.81)	140 (5.50)	3 (0.13)	168 (6.63)
317 (12)	51 (2.00)	121 (4.75)	11 (0.44)	173 (6.81)	137 (5.38)	8 (0.31)	187 (7.38)
254 (10)	54 (2.13)	116 (4.56)	13 (0.50)	175 (6.88)	137 (5.38)	8 (0.31)	187 (7.38)
203 (8)	51 (2.00)	121 (4.75)	10 (0.38)	175 (6.88)	140 (5.50)	6 (0.25)	187 (7.38)
152 (6)	51 (2.00)	127 (5.00)	6 (0.25)	171 (6.75)	140 (5.50)	3 (0.13)	184 (7.25)
102 (4)	57 (2.25)	133 (5.25)	2 (0.06)	171 (6.75)	146 (5.75)	0.0	184 (7.25)
51 (2)	N/A	N/A	0.00	171 (6.75)	162 (6.00)	0.0	184 (7.25)

was tested at a scaled standoff of  $1.71x$ , the average of two values for B6 (tested, respectively, at standoffs of  $2.29x$  and  $1.07x$ ). Moderate flattening of the front face of the specimen was observed post-test. The maximum measured lateral deformation from this first test was 37.5 mm (1.48 in.) at a height of 254 mm (10 in.).

### Test 16: Specimen B11

Specimen B11 was tested again with the same charge, but placed closer at a scaled standoff of  $1.43x$ . The cumulative deformation after the second test reached a maximum of 119 mm (4.70 in.) at 254 mm (10 in.) over the top of the foundation. Denting and bending of the specimen was once again observed, with a  $C$  value of 7.9 mm (5/16 in.).

### Test 17: Specimen B12

Specimen B12 was a modified version of B7, with a thicker outside tube (for a more compact tube), and a section more resilient to caving. The scaled standoff from Specimen B12 to the charge was  $1.29x$ . B12 deformed a full 127 mm (5.0 in.), including denting at the cross-section level. Denting of the specimen was rather important, with a  $C$  of 25.4 mm (1 in.); the reduction in diameter was as much as 38%.

### Summary of Findings: Blast Test (Internal Deformations)

In general, the CFDSTs test items showed that cross-section deformation (denting/caving) was an important deformation mechanism to absorb energy from overpressures from near-contact explosions. Thus, global deformations were reported in two formats: for sections not dented, maximum lateral bending deformation and the associated rotations at three locations (top, bottom, and point of maximum deformation); and for dented sections, the maximum lateral deformation and cross-section deformations. Further processing of the CFDST sections was performed to observe their response at the cross-section level. Some of the specimens from both the *ECLIPSE* and the ERDC tests were split open to expose their concrete core and to determine the state of the internal tube. Upon opening, it was generally observed that the face of the concrete core exposed to the blast was severely deformed or crushed, and that the concrete flowed significantly in trying to follow the deformation of the cross section (Fig. 22).

On the upper part of the specimen, horizontal flexural cracks were generally visible in the region where the concrete was on the tension side of the specimen under bending. The extent of the cracked region from one specimen to the other was fairly identical (Fig. 23).

In the dented region, the deformation of the cross section varied. Deformation of the cross section was directly linked to the state of the inner tube, the void ratio (hence, the thickness of the composite wall), and certainly to the loading seen by the specimen (Fig. 24). The less compact the inner tube, the more deformable the section was, and the more severe the cross-section indentation. At the center of the dented region (section directly facing the charge), the deformation of the cross section was generally severe for large void ratios (50% and more) and inner tubes with compactness well more than 20. For those sections, the inner tubes generally folded into themselves. For moderate void ratios (38–42%), the inner tube was more compact and would deform but not crush. This is evidenced by B2, which was tested twice and for which the inner tube did not completely collapse. For low void ratios (33% or less), the behavior of the inner tube seems to be affected by the compactness of the tube. For instance, for Specimen B5, which was tested once,

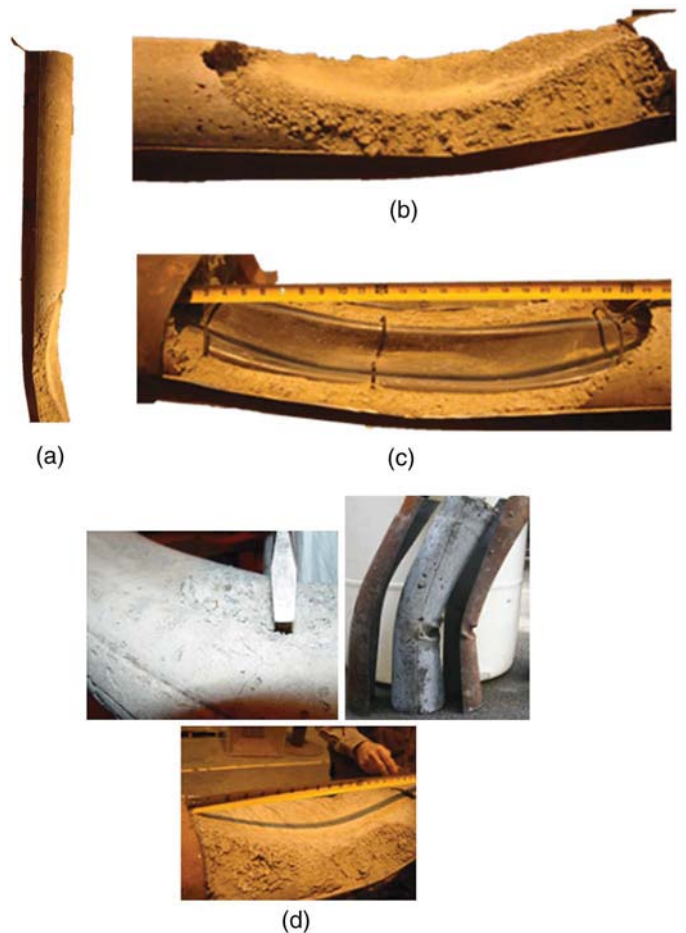


**Fig. 22.** Example opened CFDSTs: (a) location steel tube cut and removed; (b) crushed concrete; (c) inside tube after concrete removal; (d) crushed concrete removed with screwdriver and concrete *molded* to final shape of steel tube



**Fig. 23.** Crack pattern in the upper part of Specimens B5, B6, and B1

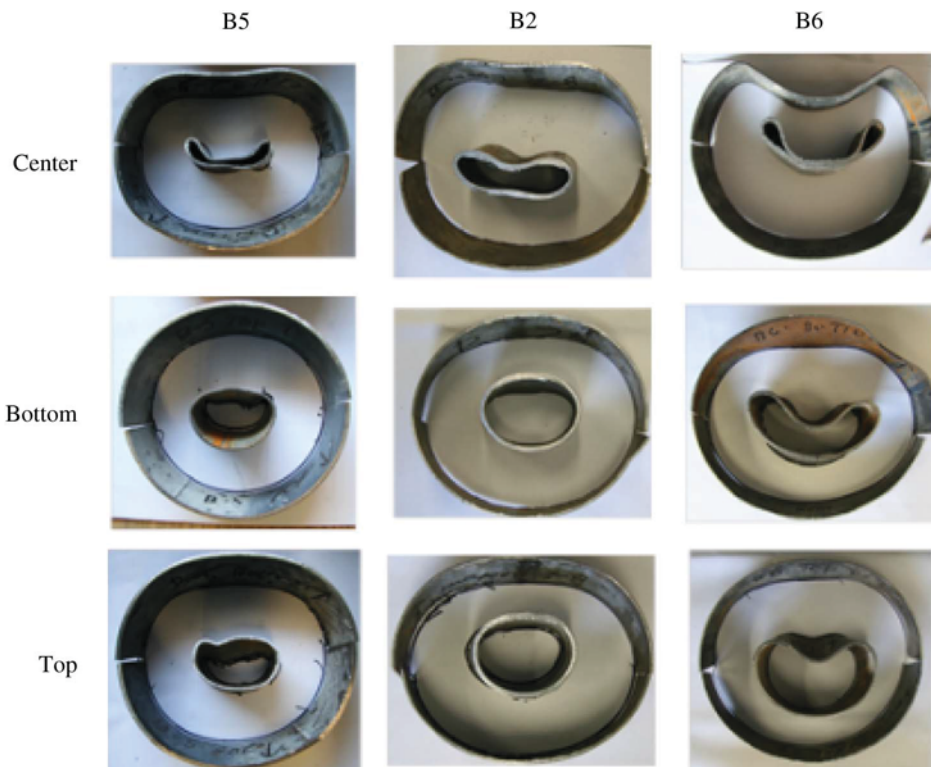


Fig. 24. Sample of cross-section deformation in the dented region

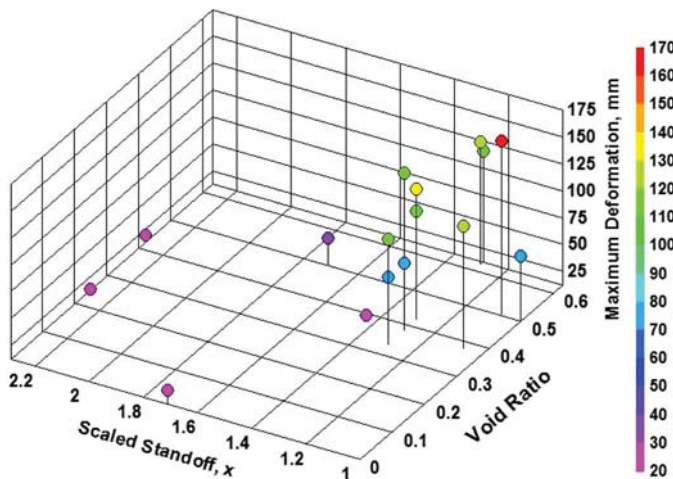


Fig. 25. Summary of all blast test deformation results as a function of the scale standoff distance and void ratios of the specimens

the compactness of the inner tube was 26%; and the inner tube collapsed into itself.

To schematically summarize the results of all blast tests, Fig. 25 shows deformations of the specimens as a function of scale standoff distance and void ratios. The development of simple analysis models able to predict these deformations will be the subject of future research.

## Conclusions

Concrete-filled double-skin tube (CFDST) columns were investigated as a promising dual-hazard-resistant concept for bridge

applications as an alternative to reinforced concrete columns in new construction. The resulting composite section is lighter than a reinforced concrete section of comparable strength and results in slimmer yet more ductile columns. The slimmer column translates into less surface to be exposed to blast overpressures. To simulate seismic response, specimens were subjected to quasi-static cyclic loading, as is commonly done in earthquake engineering studies. To investigate blast resistance, specimens were subjected to close-range explosions, with scaled distances as low as  $0.30 \text{ ft/lb}^{1/3}$  ( $0.12 \text{ m/kg}^{1/3}$ ).

In blast resistance design, local denting of the CFDST section was observed as an additional energy dissipation mechanism. In all cases tested here, CFDSTs exhibited good energy dissipation capacity and preserved their strength up to failure, under both cyclic response (simulating earthquake demands) and near-contact credible blast loads. For extreme blast events, local denting of CFDST and failure of the outside tube were observed. In such situations, the presence of the inner tube in CFDST served as a dowel that effectively prevented direct shear failure of the section. This is an important advantage compared with concrete columns (and even CFST ones).

More quantitatively, under cyclic loading, it was shown that cantilevered CFDST columns with a moderately ductile outer tube and highly ductile inner tube could reach plastic rotation well above 7% drift (0.07 rad approximately), which is similar to what has been established for CFST. However, when both the outside and inner tubes were highly ductile, section rotation of up to 0.12 rad were achievable at the base of the specimen, meaning deformations twice as large were reached at the point of maximum deformation. Under blast loading, section rotations of CFDST of 0.05 rad were observed without local denting. Denting accompanied by section rotation of up to 0.239 rad was achieved if fracture of a moderately ductile outside tube was not observed (Specimen B3). For highly ductile outer tubes, denting of the section could lead to an average

rotation at the base in excess of 0.40 rad (average of Specimens B9, B10, B11, and B12) without any fracture.

## Recommendations for Further Studies

As interest on multihazard design grows, CFST and CFDST are increasingly appealing solutions. As a consequence, advancing knowledge on their behavior is key to their adoption in multihazard applications. The following items are suggested for further research on these structural systems.

- Modeling of blast structure interaction for CFDST subjected to blast loading is needed to help optimize design parameters for both systems.
- Investigation of alternative instrumentation techniques to quantify real-time dynamic response of bridge piers under blast and impulsive loading is needed.
- Investigation of the importance of scale effects on the performance of CFDST is desirable and could be addressed by conducting 1/2-scale or full-scale tests. In particular, for larger scale CFDST, the composite wall is expected to be more resistant to denting.
- Effectiveness of adding passive infill material, such as sand or other materials, in the void of CFDST as an option to prevent cross-section distortion at extremely close scaled distances and improve energy dissipation capacity.
- Additional blast tests are desirable on CFDST and dowel-reinforced CFST to investigate resistance to contact charges and shear resistance at footings when column rotation capability is exceeded.

## Appendix. Equations to Calculate $M_p$ of CFDST

The plastic moments of the CFDST sections are calculated here, assuming that both tubes become fully plastic and that the concrete in compression has reached and sustained its crushing strength, maintaining full composite action. This is similar to the approach adopted for CFST that yielded results in good agreement with prior CFST experiments (Bruneau and Marson 2004). Equations must be derived depending on whether the plastic neutral axis (PNA) is located above or across the inner tube, per the stress distributions shown in Fig. 26. When the neutral axis is located above the inner tube, the resultant of the compressive and tensile forces maintaining the sections in equilibrium are as follow:

$$C_{ro} = (\pi - 2\beta_o)R_o t_o F_{yo} \quad (1)$$

$$C'_r = \left[ \left( \frac{\pi}{2} - \beta_o \right) R_o^2 - \frac{1}{2} R_o^2 \sin(2\beta_o) \right] f'_c \quad (2)$$

$$T_{ri} = 2\pi R_i t_i F_{yi} \quad (3)$$

$$T_{ro} = (\pi + 2\beta_o)R_o t_o F_{yo} \quad (4)$$

where  $C_{ro}$  = resultant compressive force acting on the outer tube;  $C'_r$  = resultant compressive force in the concrete;  $T_i$  = resultant tensile force on the inner tube; and  $T_{ro}$  = resultant tensile force acting on the outer tube. The corresponding points of application for the above-defined forces with respect to the geometric center of the section, respectively, are

$$y_{sco} = \frac{2R_o \cos\beta_o}{(\pi - 2\beta_o)} \quad (5)$$

$$y_c = \frac{2R_o}{3} \frac{\cos^3\beta_o}{\left(\frac{\pi}{2} - \beta_o\right) - \frac{1}{2}\sin(2\beta_o)} \quad (6)$$

$$y_{sti} = 0 \quad (7)$$

$$y_{sto} = \frac{2R_o \cos\beta_o}{(\pi + 2\beta_o)} \quad (8)$$

where  $y_{sco}$  = point of application of the resultant compressive force acting on the outer tube;  $y_c$  = point of application of the resultant compressive force in the concrete;  $y_{sti}$  = point of application of the resultant tensile force on the inner tube;  $y_{sto}$  = point of application of the resultant tensile force acting on or above the outer tube. With those parameters, the resultant axial and flexural capacities of the section are defined as

$$P = (C_{ro} + C'_r) - (T_{ri} + T_{ro}) \quad (9)$$

$$M_p = C_{ro}y_{sco} + C'_r y_c + T_{ri}y_{sti} + T_{ro}y_{sto} \quad (10)$$

Carrying out the necessary calculations leads to the following equations:

$$P = \left( \frac{\pi}{2} - \beta_o - \frac{1}{2} \sin 2\beta_o \right) R_o^2 f'_c - 4\beta_o R_o t_o F_{yo} - 2\pi R_i t_i F_{yi} \quad (11)$$

$$M_p = \frac{2}{3} R_o^3 \cos^3\beta_o f'_c + 4R_o^2 \cos\beta_o t_o F_{yo} \quad (12)$$

The location of the neutral axis for the case of pure flexure on the section is obtained by setting the axial force in the above equations to zero, leading to the mixed equation in  $\beta_o$ :

$$\begin{aligned} & (4R_o t_o F_{yo} + R_o^2 f'_c) \beta_o + \frac{1}{2} R_o^2 f'_c \sin 2\beta_o \\ & + \left( 2\pi R_i t_i F_{yi} - \frac{\pi}{2} R_o^2 f'_c \right) = 0 \end{aligned} \quad (13)$$

This equation can be solved in *Mathcad*. Alternatively, a conservative estimate can be obtained using the approximation that  $\sin\beta_o = \beta_o$  and  $\cos\beta_o = 1$ , which results in the following equation in  $\beta_o$ :

$$\beta_o = \frac{\pi R_o^2 f'_c - 4\pi R_i t_i F_{yi}}{8R_o t_o F_{yo} + 4R_o^2 f'_c} \quad (14)$$

where

$$\sin^{-1} \left( \frac{R_i}{R_o} \right) < \beta_o \leq \frac{\pi}{2} \quad (15)$$

The location of the plastic neutral axis ( $h$ ) can then be calculated using the geometry of the section as

$$h = R_o \sin\beta_o \quad (16)$$

Similar equations can be derived for a neutral axis located across the inner tube. The equations for the forces acting on the cross section and their corresponding points of application are

$$C_{ro} = (\pi - 2\beta_o)R_o t_o F_{yo} \quad (17)$$

$$C_{ri} = (\pi - 2\beta_i)R_i t_i F_{yi} \quad (18)$$

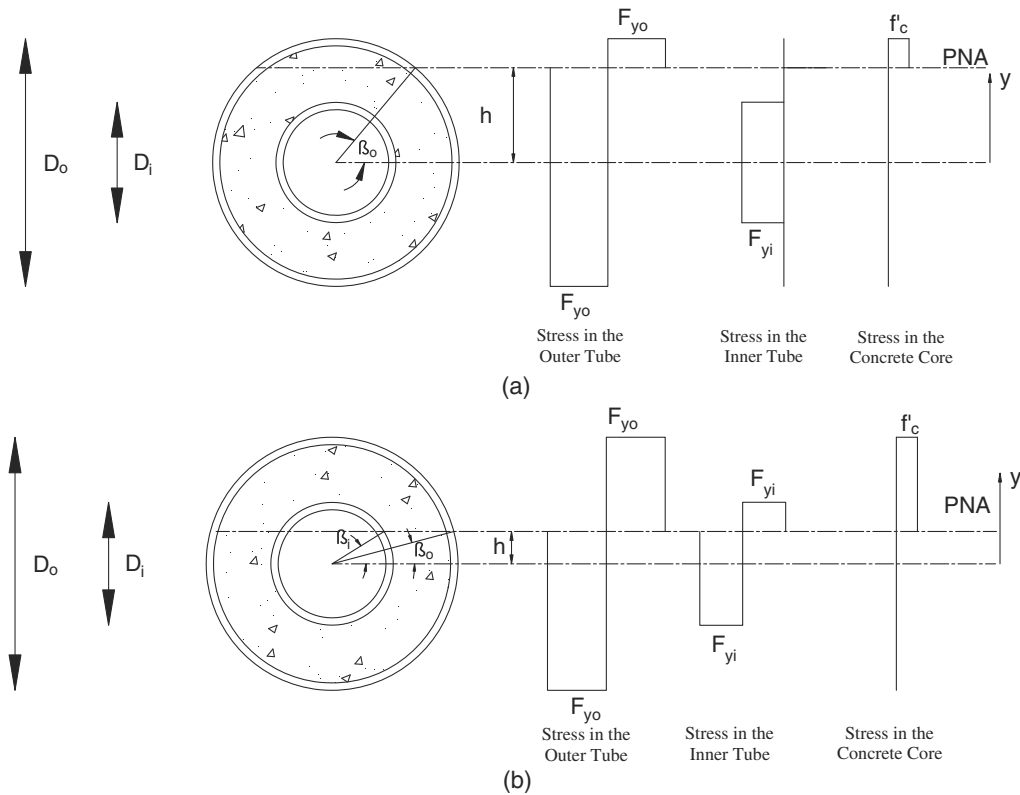


**Fig. 26.** Stress distribution at  $M_p$ : (a) PNA above inner tube; (b) PNA across inner tube

$$C'_r = \left[ \left( \frac{\pi}{2} - \beta_o \right) R_o^2 - \left( \frac{\pi}{2} - \beta_i \right) R_i^2 - \frac{1}{2} R_o^2 \sin(2\beta_o) + \frac{1}{2} R_i^2 \sin(2\beta_i) \right] f'_c \quad (19)$$

$$T_{ro} = (\pi + 2\beta_o) R_o t_o F_{yo} \quad (20)$$

$$T_{ri} = (\pi + 2\beta_i) R_i t_i F_{yi} \quad (21)$$

$$y_{sco} = \frac{2R_o \text{Cos}\beta_o}{(\pi - 2\beta_o)} \quad (22)$$

$$y_{sci} = \frac{2R_i \text{Cos}\beta_i}{(\pi - 2\beta_i)} \quad (23)$$

$$y_c = \frac{2R_o}{3} \frac{\text{Cos}^3\beta_o}{\left( \frac{\pi}{2} - \beta_o \right) - \frac{1}{2} \sin(2\beta_o)} \quad (24)$$

$$y_{sto} = \frac{2R_o \text{Cos}\beta_o}{(\pi + 2\beta_o)} \quad (25)$$

$$y_{sto} = \frac{2R_i \text{Cos}\beta_i}{(\pi + 2\beta_i)} \quad (26)$$

The axial force and moment acting on the cross section in this configuration are

$$P_u = (C_{ro} + C_{ro} + C'_r) - (T_{ri} + T_{ro}) \quad (27)$$

$$M_u = C_{ro} y_{sco} + C_{ri} y_{sci} + C'_r y_c + T_{ri} y_{sti} + T_{ro} y_{sto} \quad (28)$$

After substitutions and algebraic manipulations, the following equations are obtained:

$$P = \left[ \left( \frac{\pi}{2} - \beta_o - \frac{1}{2} \sin\beta_o \right) R_o^2 - \left( \frac{\pi}{2} - \beta_i - \frac{1}{2} \sin\beta_i \right) R_i^2 \right] f'_c - 4\beta_o R_o t_o F_{yo} - 4\beta_i R_i t_i F_{yi} \quad (29)$$

$$M_p = \frac{2}{3} (R_o^3 \cos^3\beta_o - R_i^3 \cos^3\beta_i) f'_c + 4(R_o^2 \cos\beta_o t_o F_{yo} + R_i^2 \cos\beta_i t_i F_{yi}) \quad (30)$$

As before, the location of the neutral axis for the pure flexure condition can be solved for by setting  $P_u$  to zero. The following equations in  $\beta_o$  and  $\beta_i$  are obtained:

$$(4R_o t_o F_{yo} + R_o^2 f'_c) \beta_o + (4R_i t_i F_{yi} - R_i^2 f'_c) \beta_i + \left( \frac{1}{2} R_o^2 \sin 2\beta_o - \frac{1}{2} R_i^2 \sin 2\beta_i \right) f'_c - \left( \frac{\pi}{2} R_o^2 f'_c - \frac{\pi}{2} R_i^2 f'_c \right) = 0 \quad (31)$$

$$h = R_o \sin\beta_o = R_i \sin\beta_i \quad (32)$$

Using the same approximations as above, an estimate of the plastic neutral axis location is obtained with

$$\beta_o = \frac{\pi(R_o^2 - R_i^2) f'_c}{4R_o [2(t_o F_{yo} + t_i F_{yi}) + (R_o - R_i) f'_c]} \quad (33)$$

**Table 10.** Calculated Section Neutral Axis and Strengths

Specimen	$h$ [in. (mm)]	$h_{\text{approx}}$ [in. (mm)]	Error (%)	$M_p$ [kip-in. (kN-mm)]	$M_{p,\text{approx}}$ [kip-in. (kN-mm)]	Error (%)
S1	0.93 (24)	0.88 (22)	-5.4	207.456 (23,443)	205.127 (23,179)	-1.1
S2	1.543 (39)	1.494 (38)	-3.2	514.981 (58,192)	519.743 (58,731)	0.9
S3	0.992 (25)	0.937 (24)	-5.5	446.091 (50,408)	444.284 (50,204)	-0.4
S4	0.97 (25)	0.883 (22)	-9.0	314.609 (35,551)	312.202 (35,279)	-0.8
S5	1.607 (41)	1.559 (40)	-3.0	532.50 (60,173)	529.051 (59,782)	-0.6

$$\beta_i = \frac{\pi(R_o^2 - R_i^2)f'_c}{4R_i[2(t_oF_{yo} + t_iF_{yi}) + (R_o - R_i)f'_c]} \quad (34)$$

In that case

$$0 \leq \beta_o \leq \sin^{-1}\left(\frac{R_i}{R_o}\right) \quad (35)$$

Comparisons of results obtained from the exact and approximate equations are presented in Table 10 (approximate values are with subscript approx). Results from the approximate equations are roughly within 1% of the exact ones, and conservative, with better match when the neutral axis crosses the inner tube (i.e., Specimens S1, S3, S4, and S5) and better accuracy for cases with larger void ratios.

## Acknowledgments

This research was partly supported by the Federal Highway Administration under an award to MCEER and by the Infrastructure Protection and Disaster Management Division, Science and Technology Directorate, U.S. Department of Homeland Security under a cooperative agreement with the U.S. Army Engineer Research Development Center (Contract W912HZ-11-2-0001). Any opinions, findings, conclusions, and recommendations presented in this paper are those of the authors and do not necessarily reflect the views of the sponsors. Permission to publish was granted by the Director, Geotechnical and Structures Laboratory.

## References

- AASHTO. (2012). *AASHTO guide specifications for LRFD seismic bridge design*, 2nd Ed., Washington, DC.
- ACI (American Concrete Institute). (1992). *Standard practice for selecting proportions for normal, heavyweight, and mass concrete*, Farmington Hills, MI.
- AISC. (2010). "Seismic provisions for structural steel buildings." *ANSI/AISC 341-10*, Chicago.
- API (American Petroleum Institute). (1989). *Draft recommended practice for planning, designing and constructing fixed offshore platforms. Load and resistance factor design*, Washington, DC.
- ASTM. (2015). "Standard specification for electric-resistance-welded carbon and alloy steel mechanical tubing." *ASTM A513/A513M-15*, West Conshohocken, PA.
- Baylot, J., and Rickman, D. (2007). "Uncertainties in blast loads on structures." *Structures Congress 2007*, ASCE, Reston, VA.
- Bruhl, J., and Varma, A. (2015). "Summary of blast tests on steel-plate reinforced concrete walls." *Structures Congress 2015*, ASCE, Reston, VA, 151–159.
- Bruneau, M., and Marson, J. (2004). "Seismic design of concrete-filled circular steel bridge piers." *J. Bridge Eng.*, 10.1061/(ASCE)1084-0702(2004)9:1(24), 24–34.
- Burrell, R., Aoude, H., and Saatcioglu, M. (2015). "Response of SFRC columns under blast loads." *J. Struct. Eng.*, 10.1061/(ASCE)ST.1943-541X.0001186, 04014209.
- DoD (Department of Defense). (2008). "Structures to resist the effects of accidental explosions." *UFC 3-340-02*, Washington, DC.
- FEMA. (2000). "Prestandard and commentary for the seismic rehabilitation of buildings." *FEMA 356*, Washington, DC.
- FEMA. (2004). "Design guide for improving school safety in earthquakes, floods, and high winds." *FEMA 424*, Washington, DC.
- FEMA. (2009). "Quantification of building seismic performance factors." *FEMA 695*, Washington, DC.
- Fouché, P., and Bruneau, M. (2014). "Blast and seismic resistant concrete-filled double skin tubes and modified steel jacketed bridge columns." *Rep. No. MCEER-14-004*, Univ. at Buffalo, Buffalo, NY.
- Fouché, P., Bruneau, M., and Chiarito, V. P. (2016). "Modified steel jacketed columns for combined blast and seismic retrofit of existing bridge columns." *J. Bridge Eng.*, 10.1061/(ASCE)BE.1943-5592.0000882, 04016035.
- Fujikura, S., and Bruneau, M. (2011). "Experimental investigation of seismically resistant bridge piers under blast loading." *J. Bridge Eng.*, 10.1061/(ASCE)BE.1943-5592.0000124, 63–71.
- Fujikura, S., Bruneau, M., and Lopez-Garcia, D. (2008). "Experimental investigation of multihazard resistant bridge piers having concrete-filled steel tube under blast loading." *J. Bridge Eng.*, 10.1061/(ASCE)1084-0702(2008)13:6(586), 586–594.
- Han, L.-H., Huang, H., and Zhao, X.-L. (2009). "Analytical behaviour of concrete-filled double skin steel tubular (CFDST) beam-columns under cyclic loading." *Thin-Walled Struct.*, 47(6), 668–680.
- Han, L.-H., Tao, Z., and Zhao, X. (2006). "Concrete-filled double skin steel tubular (CFDST) beam-columns subjected to cyclic bending." *Eng. Struct.*, 28(12), 1698–1714.
- Hsiao, P., Kazuhiro Hayashi, K., Nishi, R., Lin, X., and Nakashima, M. (2015). "Investigation of concrete-filled double-skin steel tubular columns with ultrahigh-strength steel." *J. Struct. Eng.*, 10.1061/(ASCE)ST.1943-54, 04014166.
- Huang, H., Han, L.-H., and Zhao, X.-L. (2013). "Investigation on concrete filled double skin steel tubes (CFDSTs) under pure torsion." *J. Constr. Steel Res.*, 90(3), 221–234.
- Huang, H., Han, L.-H., Tao, Z., and Zhao, X.-L. (2010). "Analytical behaviour of concrete-filled double skin steel tubular (CFDST) stub columns." *J. Constr. Steel Res.*, 66(4), 542–555.
- Imani, R., Mosqueda, G., and Bruneau, M. (2015a). "Experimental study on post-earthquake fire resistance of ductile concrete filled double-skin tube columns." *J. Struct. Eng.*, 10.1061/(ASCE)ST.1943-541X.0001168(2015)141(8), 04014192.
- Imani, R., Mosqueda, G., and Bruneau, M. (2015b). "Finite element simulation of concrete filled double-skin tube columns subjected to post-earthquake fires." *J. Struct. Eng.*, 10.1061/(ASCE)ST.1943-541X.0001301(2015)141(12), 04014192.
- Lin, M. L., and Tsai, K. C. (2001). "Behavior of double-skinned composite steel tubular columns subjected to combined axial and flexural loads." *1st Int. Conf. on Steel and Composite Structures*, Techno-Press, Daejeon, Korea.
- Li, W., Han, L.-H., and Chan, T.-M. (2014a). "Tensile behaviour of concrete-filled double-skin steel tubular members." *J. Constr., Steel Res.*, 99(8), 35–46.
- Li, W., Han, L.-H., and Chan, T.-M. (2014b). "Numerical investigation on the performance of concrete-filled double-skin steel tubular members under tension." *Thin-Walled Struct.*, 79, 108–118.
- Li, W., Han, L.-H., Ren, Q.-X., and Zhao, X.-L. (2013). "Behavior and calculation of tapered CFDST columns under eccentric compression." *J. Constr. Steel Res.*, 83, 127–136.

- Li, W., Ren, Q.-X., Han, L.-H., and Zhao, X.-L. (2012). "Behaviour of tapered concrete-filled double skin steel tubular (CFDST) stub columns." *Thin-Walled Struct.*, 57, 37–48.
- Lu, H., Zhao, X.-L., and Han, L.-H. (2010). "Testing of self-consolidating concrete-filled double skin tubular stub columns exposed to fire." *J. Constr. Steel Res.*, 66(8), 1069–1080.
- Mathcad [Computer software]. PTC, Needham, MA.
- Montague, P. (1975). "Simple composite construction for cylindrical shells subjected to external pressure." *J. Mech. Eng. Sci.*, 17(2), 105–113.
- Orton, S., Chiarito, V., Minor, J., and Coleman, T. (2014). "Experimental testing of CFRP-strengthened reinforced concrete slab elements loaded by close-in blast." *J. Struct. Eng.*, 10.1061/(ASCE)ST.1943-541X.0000821, 04013060.
- Pagoulatou, M., Sheehan, T., Dai, X., and Lam, D. (2014). "Finite element analysis on the capacity of circular concrete-filled double-skin steel tubular (CFDST) stub columns." *Eng. Struct.*, 72(9), 102–112.
- Shakir-Khalil, H. (1991). "Composite columns of double-skinned shells." *J. Constr. Steel Res.*, 19(2), 133–152.
- Tao, Z., and Han, L.-H. (2006). "Behavior of concrete-filled double skin rectangular steel tubular beam-columns." *J. Constr. Steel Res.*, 62(7), 631–646.
- Tao, Z., Han, L.-H., and Zhao, X.-L. (2004). "Behaviour of concrete-filled double skin (CHS inner and CHS outer) steel tubular stub columns and beam-columns." *J. Constr. Steel Res.*, 60(8), 1129–1158.
- Uenaka, K., Kitoh, H., and Sonoda, K. (2010). "Concrete filled double skin circular stub columns under compression." *Thin-Walled Struct.*, 48(1), 19–24.
- Wei, S., Mau, S. T., Vipulanandan, C., and Mantrala, S. K. (1995). "Performance of new sandwich tube under axial loading: Experiment." *J. Struct. Eng.*, 10.1061/(ASCE)0733-9445(1995)121:12(1806), 1806–1814.
- Williams, D., Holland, C., Williamson, E., Bayrak, O., Marchand, K., and Ray, J. (2008). "Blast-resistant highway bridges: Design and detailing guidelines." *Proc., 10th Int. Conf. on Structures under Shock and Impact (SUSI)*, WIT Press, Southampton, U.K.
- Williamson, E. B., and Winget, D. G. (2005). "Risk management and design of critical bridges for terrorist attacks." *J. Bridge Eng.*, 10.1061/(ASCE)1084-0702(2005)10:1(96), 96–106.
- Woodson, S. C., and Baylot, J. T. (1999). "Structural collapse: Quarter-scale model experiments." *Tech. Rep. No. SL-99-8*, U.S. Army Engineer Research and Development Center, Vicksburg, MS.
- Yuan, W., and Yang, J. (2013). "Experimental and numerical studies of short concrete-filled double skin composite tube columns under axially compressive loads." *J. Constr. Steel Res.*, 80(10), 23–31.
- Zhang, F., et al. (2016). "Experimental study of CFDST columns infilled with UHPC under close-range blast loading." *Int. J. Impact Eng.*, 93, 184–195.
- Zhao, X.-L., Tong, L.-W., and Wang, X.-Y. (2010). "CFDST stub columns subjected to large deformation axial loading." *Eng. Struct.*, 32(3), 692–703.
- Zhong, T., Han, L.-H., and Zhao, X.-L. (2004). "Behaviour of concrete-filled double skin (CHS inner and CHS outer) steel tubular stub columns and beam-columns." *J. Constr. Steel Res.*, 60(8), 1129–1158.